First observation of ^{28}O

Y Kondo, N.L Achouri, H. Al Falou, L Atar, T Aumann, H Baba, K Boretzky, C Caesar, D Calvet, H Chae, et al.

To cite this version:

Y Kondo, N.L Achouri, H. Al Falou, L Atar, T Aumann, et al.. First observation of ^{28}O. Nature, 2023, 620 (7976), pp.965-970. 10.1038/s41586-023-06352-6 . hal-04196834

HAL Id: hal-04196834
https://hal.science/hal-04196834v1

Submitted on 9 Oct 2023

First observation of ^{28}O

Y. Kondo*,[1] N.L. Achouri,[2] H. Al Falou,[3,4] L. Atar,[5] T. Aumann,[5,6,7] H. Baba,[8] K. Boretzky,[6] C. Caesar,[5,6] D. Calvet,[9] H. Chae,[10] N. Chiga,[8] A. Corsi,[9] F. Delaunay,[2] A. Delbart,[9] Q. Deshayes,[2] Zs. Dombrádi,[11] C.A. Douma,[12] A. Ekström,[13] Z. Elekes,[11] C. Forssén,[13] I. Gašparić,[14,8,5] J.-M. Gheller,[9] J. Gibelin,[2] A. Gillibert,[9] G. Hagen,[15,16] M.N. Harakeh,[6,12] A. Hirayama,[1] C.R. Hoffman,[17] M. Holl,[5,6] A. Horvat,[6] Á. Horváth,[18] J.W. Hwang,[19,20] T. Isobe,[8] W.G. Jiang,[13] J. Kahlbow,[5,8] N. Kalantar-Nayestanaki,[12] S. Kawase,[21] S. Kim,[19,20] K. Kisamori,[8] T. Kobayashi,[22] D. Körper,[6] S. Koyama,[23] I. Kuti,[11] V. Lapoux,[9] S. Lindberg,[13] F.M. Marqués,[2] S. Masuoka,[24] J. Mayer,[25] K. Miki,[22] T. Murakami,[26] M. Najafi,[12] T. Nakamura,[1] K. Nakano,[21] N. Nakatsuka,[26] T. Nilsson,[13] A. Obertelli,[9] K. Ogata,[27,28,29] F. de Oliveira Santos,[30] N.A. Orr,[2] H. Otsu,[8] T. Otsuka,[23,8] T. Ozaki,[1] V. Panin,[8] T. Papenbrock,[16,15] S. Paschalis,[5] A. Revel,[2,30] D. Rossi,[5] A.T. Saito,[1] T.Y. Saito,[23] M. Sasano,[8] H. Sato,[8] Y. Satou,[20] H. Scheit,[5] F. Schindler,[5] P. Schrock,[24] M. Shikata,[1] N. Shimizu,[31] Y. Shimizu,[8] H. Simon,[6] D. Sohler,[11] O. Sorlin,[30] L. Stuhl,[19,8] Z.H. Sun,[16,15] S. Takeuchi,[1] M. Tanaka,[32] M. Thoennessen,[33] H. Törnqvist,[6,5] Y. Togano,[34,1] T. Tomai,[1] J. Tscheuschner,[5] J. Tsubota,[1] N. Tsunoda,[24] T. Uesaka,[8] Y. Utsuno,[35] I. Vernon,[36] H. Wang,[8] Z. Yang,[8] M. Yasuda,[1] K. Yoneda,[8] and S. Yoshida[37]

[1]Department of Physics, Tokyo Institute of Technology, 2-12-1 O-Okayama, Meguro, Tokyo 152-8551, Japan. [2]LPC Caen UMR6534, Université de Caen Normandie, ENSICAEN, CNRS/IN2P3, F-14000 Caen, France. [3]Lebanese University, Beirut, Lebanon. [4]Lebanese-French University of Technology and Applied Science, Deddeh, Lebanon. [5]Institut für Kernphysik, Technische Universität Darmstadt, 64289 Darmstadt, Germany. [6]GSI Helmholtzzentrum für Schwerionenforschung, 64291 Darmstadt, Germany. [7]Helmholtz Research Academy Hesse for FAIR, 64289 Darmstadt, Germany. [8]RIKEN Nishina Center, Hirosawa 2-1, Wako, Saitama 351-0198, Japan. [9]Irfu, CEA, Université Paris-Saclay, 91191 Gif-sur-Yvette, France. [10]IBS, 55, expo-ro, yuseong-gu, Daejeon, 34126, Republic of Korea. [11]MTA Atomki, 4001 Debrecen, Hungary. [12]ESRIG, University of Groningen, Zernikelaan 25, 9747 AA Groningen, The Netherlands. [13]Institutionen för Fysik, Chalmers Tekniska Högskola, 412 96 Göteborg, Sweden. [14]Ruđer Bošković Institute,Bijenička cesta 54, 10000 Zagreb, Croatia. [15]Physics Division, Oak Ridge National Laboratory, Oak Ridge, Tennessee 37831, USA. [16]Department of Physics and Astronomy, University of Tennessee, Knoxville, TN 37996, USA. [17]Physics Division, Argonne National Laboratory, Argonne, Illinois 60439, USA. [18]Eötvös Loránd University, Pázmány Péter Sétány 1/A, H-1117 Budapest, Hungary. [19]Center for Exotic Nuclear Studies, Institute for Basic Science, Daejeon 34126, Republic of Korea. [20]Department of Physics and Astronomy, Seoul National University, Gwanak-ro, Gwanak-gu, Seoul 08826, Republic of Korea. [21]Department of Advanced Energy Engineering Science, Kyushu University, Kasuga, Fukuoka 819-0395, Japan. [22]Department of Physics, Tohoku University, Miyagi 980-8578, Japan. [23]Unversity of Tokyo, Tokyo 1130033, Japan. [24]Center for Nuclear Study, University of Tokyo, 2-1 Hirosawa, Wako, Saitama 351-0198, Japan. [25]Institut für Kernphysik, Universität zu Köln, 50937 Köln, Germany. [26]Department of Physics, Kyoto University, Kyoto 606-8502, Japan. [27]Department of Physics, Kyushu University, Fukuoka 819-0395, Japan. [28]Research Center for Nuclear Physics, Osaka University, Ibaraki, Japan. [29]Department of Physics, Osaka City University, Osaka, Japan. [30]Grand Accélérateur National d'Ions Lourds (GANIL), CEA/DRF-CNRS/IN2P3, Bvd Henri Becquerel, 14076 Caen, France. [31]Center for Computational Sciences, University of Tsukuba, 1-1-1 Tennodai, Tsukuba 305-8577, Japan. [32]Department of Physics, Osaka University, Osaka 560-0043, Japan. [33]Facility for Rare Isotope Beams, Michigan State University, East Lansing, Michigan 48824, USA. [34]Department of Physics, Rikkyo University, 3-34-1 Nishi-Ikebukuro, Toshima, Tokyo 172-8501, Japan. [35]Advanced Science Research Center, Japan Atomic Energy Agency, Tokai, Ibaraki 319-1195, Japan. [36]Department of Mathematical Sciences, Durham University, Stockton Road, Durham, DH1 3LE, UK. [37]Liberal and General Education Center, Institute for Promotion of Higher Academic Education, Utsunomiya University, Tochigi, Japan.

Subjecting a physical system to extreme conditions is one of the means often employed to obtain a better understanding and deeper insight into its organization and structure. In the case of the atomic nucleus, one such approach is to investigate isotopes that have very different neutron-to-proton (N/Z) ratios than in stable nuclei. Light neutron-rich isotopes exhibit the most asymmetric N/Z ratios and those lying beyond the limits of binding, which undergo spontaneous neutron emission and exist only as very short-lived resonances ($\sim 10^{-21}$ seconds), provide the most stringent tests of modern nuclear structure theories. Here we report on the first observation of ^{28}O and ^{27}O via their decay into ^{24}O and four and three neutrons. The ^{28}O nucleus is of particular interest as, with 8 protons and 20 neutrons, it is expected in the standard shell model picture of nuclear structure to be one of a relatively small number of so-called "doubly-magic" nuclei. Both ^{27}O and ^{28}O were found to exist as narrow low-lying resonances and their decay energies are compared here to the results of sophisticated theoretical modelling, including a large-scale shell model calculation and a newly developed statistical approach. In both cases, the underlying nuclear interactions were derived from effective field theories of quantum chromodynamics. Finally, it is shown that the cross section for the production of ^{28}O from a ^{29}F beam is consistent with it not exhibiting a closed $N = 20$ shell structure.

One of the most active areas of present day nuclear physics is the investigation of rare isotopes with large N/Z imbalances. The structure of such nuclei provides for strong tests of our theories, including most recently, sophisticated *ab initio* type approaches whereby the underlying interactions between the constituent nucleons are constructed from first principles approaches (see, for example, ref.[1]).

Owing to the strong nuclear force, nuclei remain bound to the addition of many more neutrons than protons and the most extremely N/Z asymmetries are found for light neutron-rich nuclei (Fig. 1a). Here, beyond the limits of nuclear binding — the so-called neutron dripline — nuclei can exist as very short-lived ($\sim 10^{-21}$ seconds) resonances, which decay by spontaneous neutron emission, with their energies and lifetimes dependent on the underlying structure of the system. Experimentally, such nuclei can only be reached for the lightest systems (Fig.1a), where the location of the neutron dripline has been established up to neon ($Z = 10$)[2] and the heaviest neutron unbound nucleus observed for fluorine ($Z = 9$) ^{28}F (ref.[3]). Arguably the most extreme system, if confirmed to exist as a resonance, would be the tetra-neutron for which, a narrow near threshold continuum structure has been found in a recent missing mass measurement[4]. Here we report on the direct observation of ^{28}O ($N/Z = 2.5$), which is unbound to 4 neutron decay, and of neighbouring ^{27}O (3 neutron unbound).

The nucleus ^{28}O has long been of interest[5,6] as, in the standard shell-model picture of nuclear structure, it is expected to be "doubly magic". Indeed, it is very well established that for stable and near stable nuclei the proton and neutron numbers 2, 8, 20, 28, 50, 82, 126 correspond to spherical closed shells[7,8]. Such nuclei represent a cornerstone in our understanding of the structure of the many-body nuclear system. In particular, as considerable energy is required to excite them owing to the large shell gaps, they can be considered, when modelling nuclei in their mass region, as an "inert" core with no internal degrees of freedom. Such an approach has historically enabled more tractable calculations to be made than attempting to model an A-body ($A = Z + N$) nucleus from the full ensemble of nucleons. Indeed, this approach has been a fundamental premise of the shell model methods which have enabled an extremely wide variety of structural properties of nuclei to be described with good accuracy over a number of decades (see e.g., ref.[9]).

Of the very limited number of nuclei that are expected to be doubly magic based on the classical shell closures, ^{28}O is, given its extreme N/Z asymmetry, the only one that is in principle experimentally accessible that has yet to be observed. In recent years, the doubly magic character of the two other such neutron-rich nuclei, ^{78}Ni ($Z = 28$, $N = 50$; $N/Z = 1.8$)[10] and ^{132}Sn ($Z = 50$, $N = 82$; $N/Z = 1.6$)[11], has been confirmed. The remaining candidate, two-neutron unbound nucleus ^{10}He ($Z = 2$, $N = 8$; $N/Z = 4$), has been observed as a well-defined resonance but its magicity or otherwise has yet to be established (ref.[12]).

The $N = 20$ shell closure has long been known, however, to disappear in the neutron-rich Ne, Na and Mg ($Z = 10$–12) isotopes (see, for example, refs[13,14]). This region is referred to as the "Island of Inversion" (IoI)[15], whereby the energy gap between the neutron sd- and pf-shell orbitals, rather than being well pronounced (Fig. 1b), is weakened or even vanishes and configurations with neutrons excited into the pf-shell orbitals dominate the ground state (gs) of these nuclei as shown schematically in Fig. 1c. The IoI nuclei with such configurations are well deformed, rather than spherical, and exhibit low-lying excited states. Very recently, the IoI has been shown to extend to the fluorine isotopes ^{28,29}F ($N = 19, 20$)[3,16–18] which neighbour ^{28}O. On the other hand, the last particle-bound oxygen isotope, ^{24}O has been found to be doubly magic, with a new closed shell forming at $N = 16$ (refs.[19–23]). As such, the structural character of the more neutron-rich oxygen isotopes and, in particular, ^{28}O is an intriguing question. To date, however, only ^{25,26}O ($N = 17, 18$) have been observed, as single- and two-neutron unbound systems respectively[24–27], with the latter existing as an extremely narrow, barely unbound resonance.

The present investigation focussed on the search for ^{27,28}O, produced in high-energy reactions, through the direct detection of their decay products – ^{24}O and 3 or 4 neutrons. Critical to the success of this work was the capability of the RIKEN RIBF (RI Beam Factory) to produce intense neutron dripline beams coupled to a thick active liquid hydrogen target system and a high performance multi-neutron detection array.

Experiment

The neutron-unbound ^{27,28}O were produced via proton induced nucleon knockout reactions from a 235 MeV per nucleon beam of ^{29}F. As depicted in Extended Data Fig. 1 the ^{29}F ions were characterised and tracked onto a thick (151 mm) liquid hydrogen reaction target using plastic scintillators and multi-wire drift chambers (MWDCs). The hydrogen target was surrounded by a time projection chamber (MINOS[28]) which allowed for the determination of the reaction vertex. This combination provided for both the maximum possible luminosity together with the ability to maintain a good ^{27,28}O decay energy resolution.

The forward focussed beam velocity reaction products – charged fragments and fast neutrons – were detected and their momenta determined, using the SAMURAI spectrometer[29] including the three large-area segmented plastic scintillator walls of the NeuLAND[30] and NEBULA arrays. An overall detection efficiency for the 3 and 4 neutron decay of around 2 and 0.4% was achieved for decay energies of ~0.5 MeV (Extended Data Fig. 1). The decay energies were reconstructed from the measured momenta using the invariant-mass technique with a resolution (FWHM) of around 0.2 MeV at ~0.5 MeV decay energy (see Methods).

Analysis and results

The ^{24}O fragments were identified by the magnetic rigidity, energy loss and time-of-flight derived from the SAMURAI spectrometer detectors. The neutrons incident on the NeuLAND and NEBULA arrays were identified based on the time-of-flight and energy deposited in the plastic scintillators. Importantly, the multi-neutron detection required the application of dedicated off-line analysis procedures in order to reject crosstalk (see Methods) – that is, events in which a neutron is scattered between and registered in two or more scintillators.

In the analysis, the decay neutrons were denoted n_1, n_2, $\cdots$ by ascending order of the two-body relative energy E_{0i} between ^{24}O and n_i – such that $E_{01} < E_{02} < E_{03} < E_{04}$ (Fig. 2d). The ^{28}O decay energy, E_{01234}, reconstructed from the measured momentum vectors of the five decay particles, is shown in Fig. 2a. A narrow peak is clearly observed at ~0.5 MeV and may be assigned to be the ^{28}O ground state. As a small fraction of crosstalk events could not be eliminated by the rejection procedures care must be taken to understand their contribution to the E_{01234} spectrum. In particular, ^{24}O+3n events, in which one of the neutrons creates crosstalk and is not identified as such in the analysis can mimic true ^{28}O decay. In this context, in order to provide a complete and consistent description of all the ^{24}O+xn decay energy spectra, a full Monte-Carlo simulation was constructed (see Methods). As shown in Fig. 2a the contribution from the residual cross talk events is found to be rather limited in magnitude in the ^{24}O+4n decay energy spectrum and, moreover, produces a very broad distribution .

The decay of ^{28}O was investigated by examining the correlations in the ^{24}O plus neutrons subsystems (see Methods). In particular, the three-body (^{24}O+n_1+n_2) partial decay energy E_{012} (Extended Data Fig. 2a) was reconstructed from the ^{24}O + 4n data set. The corresponding spectrum exhibits a sharp threshold peak arising from ^{26}O$_{\mathrm{gs}}$, which is known to have a decay energy of only 18(5) keV[27]. This observation clearly indicates that ^{28}O sequentially decays through ^{26}O$_{\mathrm{gs}}$ as shown by the arrows A and B in Fig. 2e.

We have also observed, in the ^{24}O+3n channel, a ^{27}O resonance for the first time, as may be seen in the four-body decay energy (E_{0123}) spectrum of Fig. 2b. As confirmed by the simulations, which are able to simultaneously describe the ^{24}O+3n and 4n decay energy spectra, the well populated peak-like structure below ~0.5 MeV corresponds to ^{28}O events where only three of the four emitted neutrons are detected. The peak at E_{0123} ~1 MeV, however, cannot be generated by such events and must arise from a ^{27}O resonance. This was confirmed by the analysis of the data acquired with a ^{29}Ne beam (see Methods and Extended Data Fig. 2e) where ^{27}O can be produced by two-proton removal but not ^{28}O as this requires the addition of a neutron. The ^{27}O resonance also decays se-

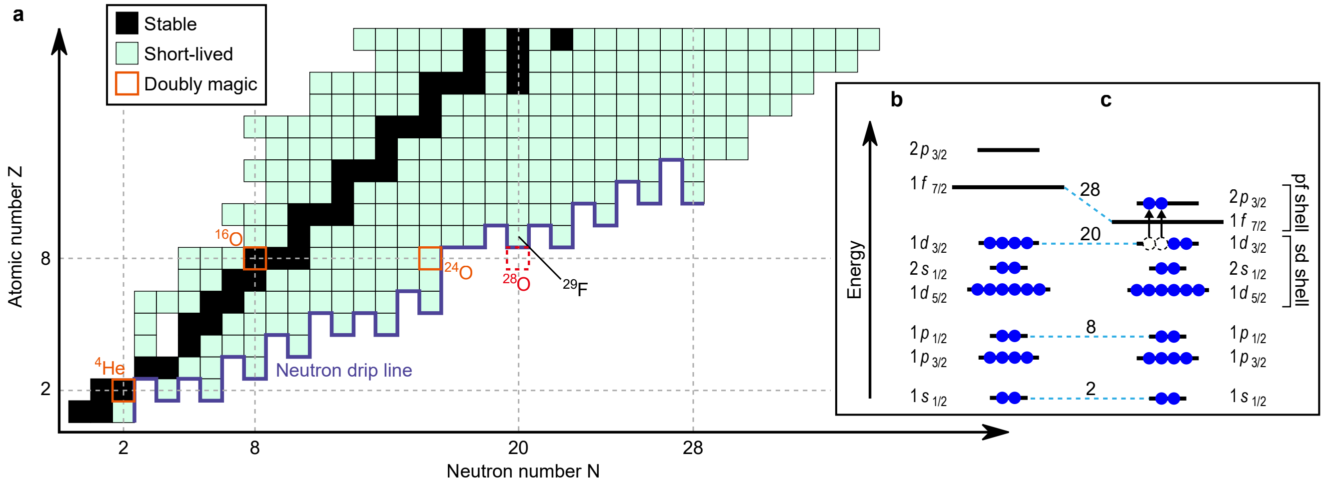

Fig. 1 | Nuclear chart and shell structure. **a**) Nuclear chart up to $Z = 18$ showing the stable and short-lived (β-decaying) nuclei. The experimentally established neutron dripline is shown by the thick blue line. Known doubly-magic nuclei are also indicated. **b**) Schematic illustration of the neutron configuration for a nucleus with a closed $N = 20$ shell. **c**) The neutron configuration involving particle-hole excitations across a quenched $N = 20$ shell gap.

quentially via $^{26}\mathrm{O}_{\mathrm{gs}}$ as shown by the arrows B and C in Fig. 2e from the analysis of the partial decay energies (Extended Data Figs.2c and d).

The decay energies of the ^{27,28}O resonances were derived from a fit of the E_{0123} spectrum with the condition that the partial decay energy satisfies $E_{012} < 0.08$ MeV (Fig. 2c) – that is, decay via the ^{26}O ground-state was selected so as to minimize the uncertainties due to contributions from higher lying ^{28}O resonances which were not identified in the present measurements owing to the limited detection efficiency (Extended Data Fig. 1). The fitting employed lineshapes which incorporated the effects of the experimental response functions, as derived from the simulations, including the contribution arising from the residual crosstalk (see Methods).

In the case of ^{28}O a decay energy of $E_{01234}=0.46^{+0.05}_{-0.04}$(stat)±0.02(syst) MeV was found with an upper limit of the width of the resonance of 0.7 MeV (68% confidence interval). The cross section for single-proton removal from ^{29}F populating the resonance was deduced to be $1.36^{+0.16}_{-0.14}$(stat)±0.13(syst) mb. The systematic uncertainties for the decay energy and the width were dominated by the precise conditions employed in the neutron crosstalk rejection procedures, while the principal contribution to that for the cross section arose from the uncertainty in the neutron detection efficiency. It may be noted that if the resonance observed here is an excited state of ^{28}O (presumably the 2^+ level), then the ground state must lie even closer to threshold and the excitation energy of the former must be less than 0.46 MeV. This, however, is very much lower than theory suggests (2 MeV or more), even when the $N = 20$ shell-closure is absent (see below). As such, it is concluded that the ground state has been observed.

In the case of ^{27}O a decay energy of E_{0123} =1.09±0.04(stat)±0.02(syst) MeV was found. The width of the resonance was comparable to the estimated experimental resolution of 0.22 MeV (FWHM). Nevertheless, it was possible to obtain an upper limit on the width – 0.18 MeV (68% confidence interval) – through a fit of a gated E_{012} spectrum for the much higher statistics ^{24}O and two-neutron coincidence events, as shown in Extended Data Fig. 2f. The spin and parity (J^{π}) of the resonance may be tentatively assigned to be $3/2^+$ or $7/2^-$ based on the upper limit of the width (see Methods).

Comparison to theory

The experimental ground-state energies of the oxygen isotopes $^{25-28}$O are summarized in Fig. 3 and compared to theoretical calculations based on chiral effective field theory (χEFT)[32,33,37–40] and large-scale shell model calculations[9,34] including those with continuum effects[35,36]. We focus on large-scale shell-model and coupled-cluster calculations, where the latter is augmented with a novel statistical method. Both techniques include explicitly three-nucleon forces which are known to play a key role in describing the structure of neutron-rich nuclei, including the oxygen isotopes and the location of the $Z = 8$ neutron dripline at ^{24}O (refs.[41–43]).

The large-scale shell model calculations were undertaken using the new EEdf3 interaction which was constructed based on χEFT (see Methods). Since the calculations employ a model space which includes the pf shell orbitals, the disappearance of the $N = 20$ shell closure can be naturally described. The EEdf3 interaction is a modified version of EEdf1[32,33], which predicts correctly the neutron dripline at F, Ne and Na, as well as a relatively low-lying ^{29}F excited state[17] and the appreciable occupancy of the neutron $2p_{3/2}$ orbital[3,18]. The EEdf3 interaction, which includes the effects of the EFT three-nucleon forces[44], provides a reasonable description of the trends in the masses of the oxygen isotopes. However, as may be seen in Fig. 3 it predicts somewhat higher ^{27,28}O energies (~1 MeV) than found in the experiment. The calculated sum of the occupation numbers for the neutron pf-shell orbitals is 2.5 (1.4) for ^{28}O (^{27}O) and for the $1d_{3/2}$ orbital 2.0 (2.1), which are consistent with a collapse of the $N = 20$ shell closure. The EEdf3 calculations show that $^{28}\mathrm{O}_{\mathrm{gs}}$ has large admixtures of configurations involving neutron excitations in the pf-shell orbitals as expected for nuclei in the IoI. This is supported by the measured cross section as discussed below.

First-principle calculations were performed using the

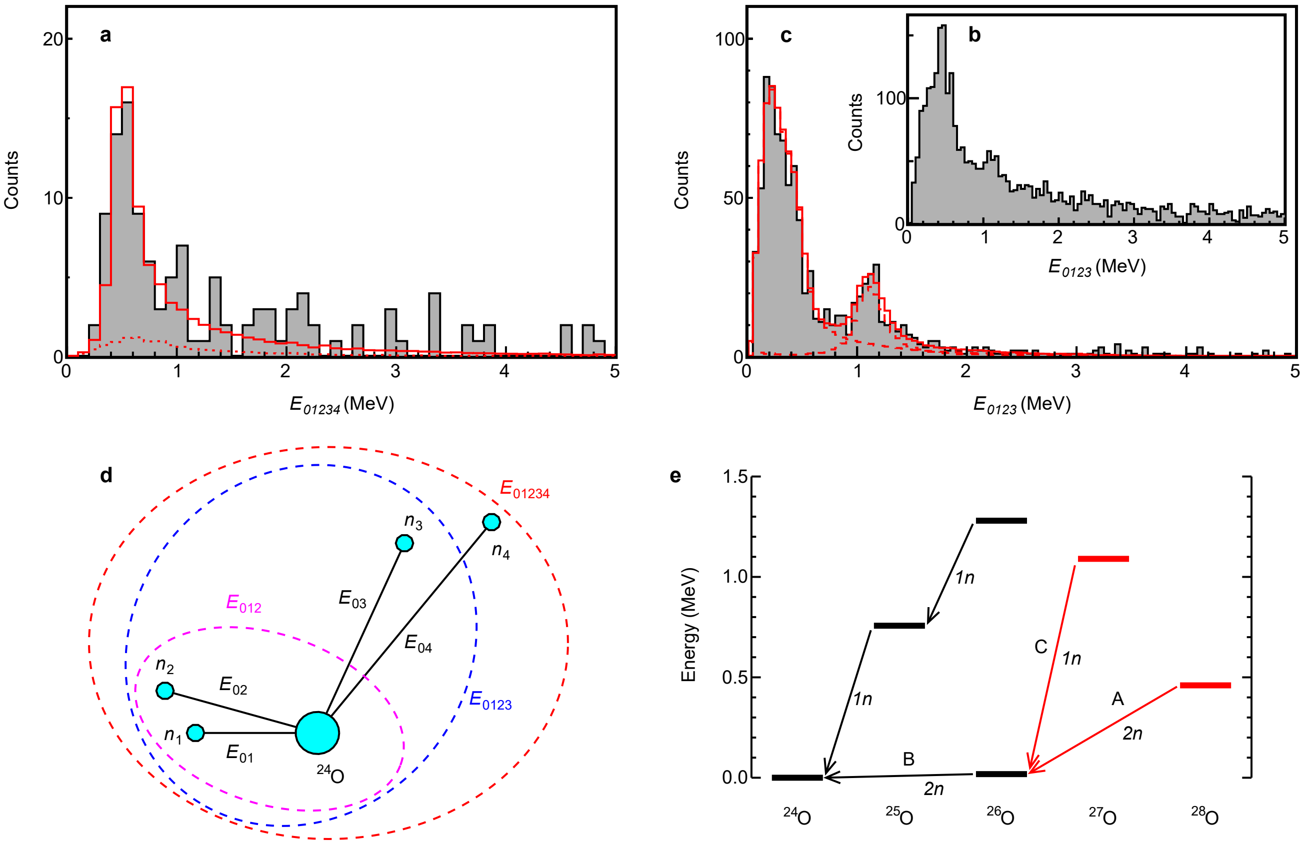

Fig. 2 | Decay energy spectra and decay scheme. a) Five-body decay energy (E_{01234}) spectrum for ^{24}O+4n events. The red-solid histogram shows the best-fit result taking into account the experimental response function. The dotted histogram shows the contribution arising from residual crosstalk that survives the rejection procedures (see Methods). **b**) Four-body decay energy (E_{0123}) spectrum for ^{24}O+3n events. **c**) Same as b, but gated by the partial decay energy $E_{012} < 0.08$ MeV. The red-dashed histograms represent the contributions from ^{28}O and ^{27}O events, and the red-solid histogram shows the sum. **d**) Definition of the partial decay energies. **e**) Decay scheme of the unbound oxygen isotopes. The newly observed resonances and their decays are shown in red.

coupled-cluster (CC) method guided by history matching (HM)[45–47] to explore the parameter space of the 17 low-energy constants (LECs) in the χEFT description of the two- and three-nucleon interactions. HM identifies the region of parameter space for which the emulated CC method generates non-implausible results (see Methods). A reliable low-statistic sample of 121 different LEC parameterizations was extracted for which the CC posterior predictive distribution (ppd) was computed for the ground-state energies of ^{27,28}O, which are shown in Fig. 3. The predicted ^{27,28}O energies are correlated, as is clearly seen in the plot of energy distributions displayed in Extended Data Fig. 3. From this, the median values and 68% credible regions were obtained for the ^{27}O–^{28}O and ^{28}O–^{24}O energy differences: $\Delta E(^{27,28}\mathrm{O})=0.11^{-0.39}_{+0.36}$ MeV and $\Delta E(^{28,24}\mathrm{O})=2.1^{-1.3}_{+1.2}$ MeV. The experimental values $\Delta E(^{27,28}\mathrm{O})=0.63\pm0.06(\mathrm{stat})\pm0.03(\mathrm{syst})$ MeV and $\Delta E(^{28,24}\mathrm{O})=0.46^{+0.05}_{-0.04}(\mathrm{stat})\pm0.02(\mathrm{syst})$ MeV, located at the edge of the 68% credible region, are consistent with the CC ppd. However, it is far enough away from the maximum to suggest that only a few finely-tuned chiral interactions may be able to reproduce the ^{27}O and ^{28}O energies. In addition, the obtained credible regions of the ^{27,28}O energies with respect to ^{24}O are relatively large, demonstrating that the measured decay energies of the extremely neutron-rich isotopes ^{27,28}O are valuable anchors for theoretical approaches based on χEFT.

In Fig. 3 the predictions of a range of other models are displayed. The USDB[9] effective interaction (constructed within the *sd* shell) provides for arguably the most reliable predictions of the properties of *sd*-shell nuclei. The continuum shell model (CSM)[35] and the Gamow shell model (GSM)[36] include the effects of the continuum, which should be important for dripline and unbound nuclei. The shell-model calculation employing the SDPF-M interaction[34] includes the *pf* shell orbitals in its model space, which should be important if either or both ^{27,28}O lie within the IoI. All the calculations, except those with the SDPF-M interaction, predict a $J^{\pi} = 3/2^{+}$ $^{27}\mathrm{O}_{\mathrm{gs}}$. In the case of the SDPF-M, a $3/2^{-}$ ground state is found with essentially degenerate $3/2^{+}$ (energy plotted in Fig. 3) and $7/2^{-}$ excited states at 0.71 MeV.

The remaining theoretical predictions are based on χEFT interactions. The valence-space in-medium similarity renormalization group (VS-IMSRG)[37] employs the 1.8/2.0 (EM) EFT potential[44]. The results for the self-consistent Green's function (SCGF) approach are shown for the NNLO$_{\mathrm{sat}}$[48] and NN+3N(lnl) potentials[38]. The coupled-cluster calculation (Λ-CCSD(T)[39]) using NNLO$_{\mathrm{sat}}$ is also shown. Except for the results obtained using the GSM, all of the calculations shown predict higher energies than found here for ^{27}O and ^{28}O.

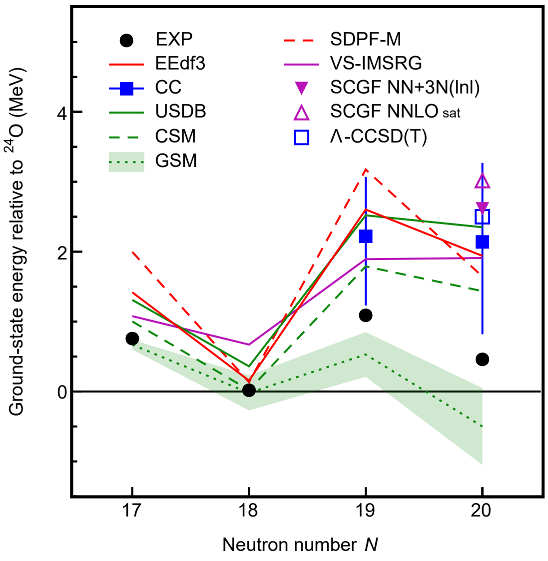

Fig. 3 | Ground-state energies with respect to ^{24}O. Experiment is shown by the filled circles where the values for ^{27,28}O are the present results and those for ^{25,26}O are taken from the atomic mass evaluation[31]. The experimental uncertainties are smaller than the symbol size. Comparison is made with predictions of shell-model calculations employing the EEdf3[32,33], USDB[9] and SDPF-M[34] (see text for ^{27}O) interactions, the coupled-cluster method with the statistical approach (CC) and shell-model calculations incorporating continuum effects (CSM[35] and GSM[36]). Also shown are the predictions of *ab initio* approaches (VS-IMSRG[37], SCGF[38], and Λ-CCSD(T)[39]). The vertical bars for CC denote 68% credible intervals. The shaded band for GSM shows the uncertainties owing to pf-continuum couplings.

We now turn to the question of whether the $N = 20$ shell closure occurs in ^{28}O. Specifically, the measured cross section for single-proton removal from ^{29}F may be used to deduce the corresponding spectroscopic factor (C^2S) – a measure of the degree of overlap between initial and final state wave functions. As noted in the Introduction, the $N = 20$ shell closure disappears in ^{29}F and the ground state is dominated by neutron pf-shell configurations[3,16–18]. As such, if the neutron configuration of ^{28}O is very similar to ^{29}F and the $Z = 8$ shell closure is rigid, the spectroscopic factor for proton removal will be close to unity. The spectroscopic factor was deduced using the distorted-wave impulse approximation (DWIA) approach (see Methods). As recent theoretical calculations predict $J^\pi = 5/2^+$ or $1/2^+$ for ^{29}F$_{gs}$ (see, for example, refs.[3,32,33,49–51]), the momentum distribution has been investigated (Extended Data Fig. 4) and was found to be consistent with proton removal from the $1d_{5/2}$ orbital (see Methods), leading to a $5/2^+$ assignment. The ratio of the measured to theoretical single-particle cross section provides for an experimentally deduced spectroscopic factor of $C^2S=0.48^{+0.05}_{-0.06}$(stat)±0.05(syst). Such an appreciable strength indicates that the ^{28}O neutron configuration resembles quite strongly that of ^{29}F. This value may be compared to that of 0.68 derived from the EEdf3 shell model calculations (where the center-of-mass correction factor[52] $(29/28)^2$ has been applied). The 30% difference between the experimental C^2S as compared to theory, is in line with the well-known reduction factor observed in (p, 2p) and (e, $e'p$) reactions[53]. Importantly, the EEdf3 calculations predict admixtures of the ground state wave function of ^{29}F with sd-closed-shell configurations of only some 12%. Consequently, even when the neutrons in ^{28}O are confined to the sd shell a spectroscopic factor of only 0.13 is obtained. As such, it is concluded that, as in ^{29}F, the pf-shell neutron configurations play a major role in ^{28}O and that the $N = 20$ shell closure disappears. Consequently the IoI extends to ^{28}O and it is not a doubly-magic nucleus.

More effort will be required to properly quantify the character of the structure of ^{28}O and the neutron pf-shell configurations. In this context, the determination of excitation energy of the first 2^+ state is the next step which may be envisaged experimentally[17]. The EEdf3 calculations predict an excitation energy of 2.097 MeV, which is close to that of ~2.5 MeV computed by the particle rotor model assuming moderate deformation[54]. Both predictions are much lower than the energies found in doubly-magic nuclei – e.g., 6.917 MeV in ^{16}O and 4.7 MeV in ^{24}O (refs.[21,23]). A complementary probe of the neutron $sd-pf$-shell gap, which is within experimental reach, is the energy difference between the positive- and negative-parity states of ^{27}O as seen in ^{28}F (ref.[3]).

Conclusions

We have reported here on the first observation of the extremely neutron-rich oxygen isotopes ^{27,28}O. Both nuclei were found to exist as relatively low-lying resonances. These observations were made possible using a state-of-the-art setup which permitted the direct detection of 3 and 4 neutrons. From an experimental point of view, the multi-neutron-decay spectroscopy demonstrated here opens up new perspectives in the investigation of other extremely neutron-rich systems lying beyond the neutron dripline and the study of multi-neutron correlations. Comparison of the measured energies of ^{27,28}O with respect to ^{24}O with a broad range of theoretical predictions, including two approaches employing nuclear interactions derived from effective field theories of quantum chromodynamics, showed that in almost all cases theory underbinds both systems. The statistical coupled-cluster calculations indicated that the energies of ^{27,28}O can provide valuable constraints of such *ab initio* approaches and, in particular, the interactions employed. Finally, while ^{28}O is expected in the standard shell-model picture to be a doubly-magic nucleus ($Z = 8$ and $N = 20$), the single-proton removal cross section measured here, when compared to theory, was found to be consistent with it not having a closed neutron shell character. This result suggests that the island of inversion extends beyond ^{28,29}F into the oxygen isotopes.

1. Hergert, H. A Guided Tour of ab initio Nuclear Many-Body Theory. Front. Phys. **8**, (2020).
2. Ahn, D. S. *et al.* Location of the Neutron Dripline at Fluorine and Neon. Phys. Rev. Lett. **123**, 212501 (2019).
3. Revel, A. *et al.* Extending the Southern Shore of the Island of Inversion to ^{28}F. Phys. Rev. Lett. **124**, 152502 (2020).
4. Duer, M. *et al.* Observation of a correlated free four-neutron system. Nature **606**, 678–682 (2022).
5. Sakurai, H. *et al.* Evidence for particle stability of ^{31}F and particle instability of ^{25}N and ^{28}O. Phys. Lett. B **448**, 180–184 (1999).

6. Tarasov, O. *et al.* Search for ^{28}O and study of neutron-rich nuclei near the $N = 20$ shell closure. Phys. Lett. B **409**, 64–70 (1997).
7. Mayer, M. G. On Closed Shells in Nuclei. II. Phys. Rev. **75**, 1969–1970 (1949).
8. Haxel, O., Jensen, J. H. D. & Suess, H. E. On the "Magic Numbers" in Nuclear Structure. Phys. Rev. **75**, 1766–1766 (1949).
9. Brown, B. A. & Richter, W. A. New "USD" Hamiltonians for the *sd* shell. Phys. Rev. C **74**, 034315 (2006).
10. Taniuchi, R. *et al.* ^{78}Ni revealed as a doubly magic stronghold against nuclear deformation. Nature **569**, 53–58 (2019).
11. Jones, K. L. *et al.* The magic nature of ^{132}Sn explored through the single-particle states of ^{133}Sn. Nature **465**, 454–457 (2010).
12. Matta, A. *et al.* New findings on structure and production of ^{10}He from ^{11}Li with the $(d,^{3}\text{He})$ reaction. Phys. Rev. C **92**, 041302(R) (2015). and references therein.
13. Orr, N. A. *et al.* New mass measurements of neutron-rich nuclei near N=20. Phys. Lett. B **258**, 29–34 (1991).
14. Otsuka, T., Gade, A., Sorlin, O., Suzuki, T. & Utsuno, Y. Evolution of shell structure in exotic nuclei. Rev. Mod. Phys. **92**, 015002 (2020).
15. Warburton, E. K., Becker, J. A. & Brown, B. A. Mass systematics for A=29–44 nuclei: The deformed A∼32 region. Phys. Rev. C **41**, 1147–1166 (1990).
16. Gaudefroy, L. *et al.* Direct Mass Measurements of ^{19}B, ^{22}C, ^{29}F, ^{31}Ne, ^{34}Na and Other Light Exotic Nuclei. Phys. Rev. Lett. **109**, 202503 (2012).
17. Doornenbal, P. *et al.* Low-Z shore of the "island of inversion" and the reduced neutron magicity toward ^{28}O. Phys. Rev. C **95**, 041301 (2017).
18. Bagchi, S. *et al.* Two-Neutron Halo is Unveiled in ^{29}F. Phys. Rev. Lett. **124**, 222504 (2020).
19. Ozawa, A., Kobayashi, T., Suzuki, T., Yoshida, K. & Tanihata, I. New Magic Number, $N = 16$, near the Neutron Drip Line. Phys. Rev. Lett. **84**, 5493–5495 (2000).
20. Otsuka, T. *et al.* Magic Numbers in Exotic Nuclei and Spin-Isospin Properties of the *NN* Interaction. Phys. Rev. Lett. **87**, 082502 (2001).
21. Hoffman, C. R. *et al.* Evidence for a doubly magic ^{24}O. Phys. Lett. B **672**, 17–21 (2009).
22. Kanungo, R. *et al.* One-Neutron Removal Measurement Reveals ^{24}O as a New Doubly Magic Nucleus. Phys. Rev. Lett. **102**, 152501 (2009).
23. Tshoo, K. *et al.* $N = 16$ Spherical Shell Closure in ^{24}O. Phys. Rev. Lett. **109**, 022501 (2012).
24. Hoffman, C. R. *et al.* Determination of the $N = 16$ Shell Closure at the Oxygen Drip Line. Phys. Rev. Lett. **100**, 152502 (2008).
25. Lunderberg, E. *et al.* Evidence for the Ground-State Resonance of ^{26}O. Phys. Rev. Lett. **108**, 142503 (2012).
26. Caesar, C. *et al.* Beyond the neutron drip line: The unbound oxygen isotopes ^{25}O and ^{26}O. Phys. Rev. C **88**, 034313 (2013).
27. Kondo, Y. *et al.* Nucleus ^{26}O: A Barely Unbound System beyond the Drip Line. Phys. Rev. Lett. **116**, 102503 (2016).
28. Obertelli, A. *et al.* MINOS: A vertex tracker coupled to a thick liquid-hydrogen target for in-beam spectroscopy of exotic nuclei. Eur. Phys. J. A **50**, 8 (2014).
29. Kobayashi, T. *et al.* SAMURAI spectrometer for RI beam experiments. Nucl. Instrum. Methods Phys. Res., Sect. B **317**, 294–304 (2013).
30. Boretzky, K. *et al.* NeuLAND: The high-resolution neutron time-of-flight spectrometer for R3B at FAIR. Nucl. Instrum. Methods Phys. Res., Sect. A **1014**, 165701 (2021).
31. Wang, M., Huang, W., Kondev, F., Audi, G. & Naimi, S. The AME 2020 atomic mass evaluation (II). Tables, graphs and references. Chinese Physics C **45**, 030003 (2021).
32. Tsunoda, N. *et al.* Exotic neutron-rich medium-mass nuclei with realistic nuclear forces. Phys. Rev. C **95**, 021304 (2017).
33. Tsunoda, N. *et al.* The impact of nuclear shape on the emergence of the neutron dripline. Nature **587**, 66–71 (2020).
34. Utsuno, Y., Otsuka, T., Mizusaki, T. & Honma, M. Varying shell gap and deformation in $N \sim 20$ unstable nuclei studied by the Monte Carlo shell model. Phys. Rev. C **60**, 054315 (1999).
35. Volya, A. & Zelevinsky, V. Continuum shell model. Phys. Rev. C **74**, 064314 (2006).
36. Fossez, K., Rotureau, J., Michel, N. & Nazarewicz, W. Continuum effects in neutron-drip-line oxygen isotopes. Phys. Rev. C **96**, 024308 (2017).
37. Stroberg, S. R., Holt, J. D., Schwenk, A. & Simonis, J. Ab Initio Limits of Atomic Nuclei. Phys. Rev. Lett. **126**, 022501 (2021).
38. Somà, V., Navrátil, P., Raimondi, F., Barbieri, C. & Duguet, T. Novel chiral Hamiltonian and observables in light and medium-mass nuclei. Phys. Rev. C **101**, 014318 (2020).
39. Hagen, G., Hjorth-Jensen, M., Jansen, G. R. & Papenbrock, T. Emergent properties of nuclei from *ab* initio coupled-cluster calculations. Phys. Scr. **91**, (2016).
40. Bogner, S. K. *et al.* Nonperturbative Shell-Model Interactions from the In-Medium Similarity Renormalization Group. Phys. Rev. Lett. **113**, 142501 (2014).
41. Otsuka, T., Suzuki, T., Holt, J. D., Schwenk, A. & Akaishi, Y. Three-Body Forces and the Limit of Oxygen Isotopes. Phys. Rev. Lett. **105**, 032501 (2010).
42. Hagen, G., Hjorth-Jensen, M., Jansen, G. R., Machleidt, R. & Papenbrock, T. Continuum Effects and Three-Nucleon Forces in Neutron-Rich Oxygen Isotopes. Phys. Rev. Lett. **108**, 242501 (2012).
43. Holt, J., Menéndez, J. & Schwenk, A. Chiral three-nucleon forces and bound excited states in neutron-rich oxygen isotopes. Eur. Phys. J. A **49**, (2013).
44. Hebeler, K., Bogner, S. K., Furnstahl, R. J., Nogga, A. & Schwenk, A. Improved nuclear matter calculations from chiral low-momentum interactions. Phys. Rev. C **83**, 031301 (2011).
45. Vernon, I., Goldstein, M. & Bower, R. G. Galaxy formation: a Bayesian uncertainty analysis. Bayesian Anal. **5**, 619–669 (2010).
46. Vernon, I., Goldstein, M. & Bower, R. Galaxy Formation: Bayesian History Matching for the Observable Universe. Statist. Sci. **29**, 81–90 (2014).
47. Vernon, I. *et al.* Bayesian uncertainty analysis for complex systems biology models: emulation, global parameter searches and evaluation of gene functions. BMC Systems Biology **12**, 1 (2018).
48. Ekström, A. *et al.* Accurate nuclear radii and binding energies from a chiral interaction. Phys. Rev. C **91**, 051301 (2015).
49. Utsuno, Y. *et al.* Shape transitions in exotic Si and S isotopes and tensor-force-driven Jahn-Teller effect. Phys. Rev. C **86**, 051301(R) (2012).
50. Caurier, E., Nowacki, F. & Poves, A. Merging of the islands of inversion at $N = 20$ and $N = 28$. Phys. Rev. C **90**, 014302 (2014).
51. Fossez, K. & Rotureau, J. Density matrix renormalization group description of the island of inversion isotopes $^{28\text{–}33}$F. Phys. Rev. C **106**, 034312 (2022).
52. Dieperink, A. E. L. & de Forest, T. Center-of-mass effects in single-nucleon knock-out reactions. Phys. Rev. C **10**, 543–549 (1974).
53. Wakasa, T., Ogata, K. & Noro, T. Proton-induced knockout reactions with polarized and unpolarized beams. Prog. Part. Nucl. Phys. **96**, 32–87 (2017).
54. Macchiavelli, A. *et al.* Structure of ^{29}F in the rotation-aligned coupling scheme of the particle-rotor model. Phys. Lett. B **775**, 160–162 (2017).

METHODS

Production of the ^{29}F beam The beam of ^{29}F ions was provided by the RI Beam Factory operated by the RIKEN Nishina Center and the Center for Nuclear Study (CNS), University of Tokyo. It was produced by projectile fragmentation of an intense 345 MeV per nucleon ^{48}Ca beam on a 15-mm-thick beryllium target. The secondary beam, including ^{29}F, was prepared using the BigRIPS[55] fragment separator operated with aluminum degraders of 15-mm and 7-mm median thicknesses at the first and fifth intermediate focal planes, respectively. The primary ^{48}Ca beam intensity was typically 3×10^{12} particles per second. The average intensity of the ^{29}F beam was 90 particles per second.

Measurement with a ^{29}Ne beam Data was also acquired to measure the direct population of ^{27}O via two-proton removal from ^{29}Ne. The beam was produced in a similar manner to that for ^{29}F and the energy was 228 MeV per nucleon with an average intensity of 8×10^{3} particles per second.

Unfortunately, in this measurement the cross section for the two-proton removal was much lower than expected and the statistics obtained for ^{24}O+3n coincidence events was too low to be usefully exploited. Nevertheless, the decay of ^{27}O could be identified from the ^{24}O+2n coincidence data. As may be seen in Extended Data Fig. 2e, the three-body decay energy (E_{012}) spectrum gated by $E_{01} < 0.08$ MeV – corresponding to selection of the ^{26}O ground-state decay – exhibits a clear peak at around 1 MeV. As the simulations demonstrate, this is consistent with the sequential decay of the ^{27}O resonance observed in the ^{29}F beam data (Fig. 2c).

Invariant-mass method The invariant mass of ^{28}O, $M(^{28}\text{O})$, was reconstructed from the momentum vectors of all the decay particles (^{24}O and 4n) with $M(^{28}\text{O}) = \sqrt{(\sum E_i)^2 - (\sum \boldsymbol{p}_i)^2}$, where E_i and $\boldsymbol{p}_i$ denote the total energy and momentum vector of the decay particles. The decay energy is then obtained as $E_{01234} = M(^{28}\text{O}) - M(^{24}\text{O}) - 4M_n$, where $M(^{24}\text{O})$ and M_n are the masses of ^{24}O and the neutron, respectively. The decay energy resolution is estimated by Monte-Carlo simulations. The resolution (FWHM) varies as a function of the decay energy approximately as $0.14(E_{01234} + 0.87)^{0.81}$ MeV.

Simulations The experimental response functions, for both the full and partial decay energy spectra, were derived from a Monte-Carlo simulation based on GEANT4 (ref.[56]). All relevant characteristics of the setup (geometrical acceptances and detector resolutions) were incorporated, as well as those of the beam, target and reaction effects. The QGSP_INCLXX physics class was adopted to describe the interactions of the neutrons in the detectors (as well as non active material) as it reproduces well the experimentally determined single-neutron detection efficiency as well as the detailed characteristics of neutron crosstalk events[57,58]. The generated events treated using the same analysis procedure as for the experimental data. The overall efficiency as a function of decay energy for detecting ^{24}O and 3 and 4 neutrons, as estimated by the simulations, is shown by the insets of Extended Data Fig. 1.

Fitting of decay energy spectra The energies, widths, and amplitudes of the resonances, as modelled by intrinsic lineshapes with a Breit-Wigner form with energy-dependent widths, were obtained via fits of the corresponding decay energy spectra using the maximum likelihood method, where the experimental responses were obtained by the simulations. As the decays of both ^{27}O and ^{28}O proceed via the ^{26}O ground state (18 keV[27]), the width of which is very small, the observed widths will be dominated by the one- and two-neutron decay, respectively, to ^{26}O. We assume an E_{01234}^2 dependence of the width for the 2n emission[59] to ^{26}O in the case of ^{28}O and an energy dependence for the width of the single-neutron emission[60] from ^{27}O to ^{26}O. Fits with orbital angular momentum (L) dependent widths ($L = 2$ and 3) for the latter gave consistent results within the statistical uncertainties.

A non-resonant component is not included in the fitting as it is small, if not negligible, as in the cases of ^{25,26}O produced in one-proton removal reactions in previous experiments[24–27]. The event selection with $E_{012} < 0.08$ MeV should further reduce any such contribution. As a quantitative check, a fit with a non-resonant component — modelled with a lineshape given by $p_0\sqrt{E_{0123}}\exp(-p_1E_{0123})$, where p_0 and p_1 are fitting parameters — has been examined. This gives 8% reduction in the ^{28}O cross section with a very limited impact on the energies and widths of the ^{27,28}O resonances.

Neutron crosstalk A single beam velocity neutron may scatter between individual plastic scintillator detectors of the three neutron walls of the setup. Such crosstalk events can mimic true multi-neutron events and present a source of background. By examining the apparent kinematics of such events and applying so-called causality conditions, this background can be almost completely eliminated[57,58]. Importantly, both the rejection techniques and the rate and characteristics of the crosstalk have been benchmarked in and compared to the simulations for dedicated measurements with single-neutron beams.

In the case of the 4 neutron detection to identify ^{28}O only some 16% of the events arise from crosstalk which could not be eliminated (Fig. 2a). The vast majority of these residual crosstalk events arise in cases when one (or occasionally more) of the neutrons emitted in the decay of ^{28}O is subject to crosstalk. A very much smaller fraction is also estimated to be produced when one of the three neutrons from the decay of ^{27}O, produced directly by proton and neutron knockout, undergoes crosstalk. Importantly the crosstalk cannot generate a narrow peak-like structure in the E_{01234} decay energy spectrum.

Partial decay energy of subsystems The partial decay energies of the ^{24}O+xn subsystems can be used to investigate the manner in which ^{27,28}O decay. In this analysis the decay neutrons are numbered (n_1, n_2, $\cdots$) by ascending order of two-body relative energy E_{0i} between ^{24}O and n_i – that is, such that, $E_{01} < E_{02} < E_{03} < E_{04}$. Of particular interest here is the extremely low decay energy of the ^{26}O ground state (18 keV[27]), such that it appears just above zero energy (or neutron-decay threshold) in the two-body partial decay energy E_{01} and three-body partial decay energy (E_{012}).

Extended Data Figs. 2a and b display the distributions of the partial decay energies E_{012} and E_{034} for the ^{24}O+4n coincidence events with a total decay energy $E_{01234} < 1$ MeV. The resulting sharp threshold peak in the E_{012} spectrum is a clear sign of sequential decay through the ^{26}O ground state. This is confirmed quantitatively by a simulation assuming two-neutron emission to the the ^{26}O ground state, which in turn decays by two-neutron emission to the ^{24}O ground state, which describes well the E_{012} and E_{034} spectra. By comparison, a simulation assuming five-body phase space decay fails to reproduce both of these spectra. We thus conclude that the ^{28}O ground state sequentially decays via the ^{26}O ground state as depicted in Fig. 2e.

In a similar vein the sequential decay of ^{27}O through the ^{26}O ground state was identified from the analysis of the partial decay energies for the ^{24}O+3n coincidence events. Extended Data Figs. 2c and d show the distributions of the partial decay energies E_{012} and E_{03} for events for which $1.0 < E_{0123} <$ 1.2 MeV. The E_{012} spectrum exhibits a strong enhancement at zero energy indicative of sequential decay through the ^{26}O ground state. This interpretation is confirmed by the comparison shown with a simulation for the sequential decay of ^{27}O including the contribution from the decay of ^{28}O.

Widths of the ^{27,28}O resonances As the energy of the ^{28}O resonance is lower than those of ^{27}O and ^{25}O (Fig. 2e), both one- and three-neutron emission are energetically forbidden. The two-neutron decay to the ^{26}O ground state and the four-neutron decay to ^{24}O are allowed with nearly equal decay energies. The former decay should be favoured as the effective few-body centrifugal barrier increases according to the number of emitted particles[59]. It may be noted that the upper limit of 0.7 MeV observed here for the ^{28}O resonance width is consistent with the theoretical estimates for its sequential decay[59].

The upper limit for the ^{27}O width (0.18 MeV) may be compared to the single-particle widths[61] for neutron decay. Since the width of ^{26}O is very narrow due to the extremely small decay energy (18 keV[27]), the ^{27}O width should be dominated by the one for the first step $^{27}\text{O}\rightarrow^{26}\text{O}+n$. The widths for s, p, d, f-wave neutron emission are 5, 3, 0.8, 0.06 MeV. Assuming that the corresponding spectroscopic factors are not small ($\gtrsim 0.1$), this would suggest that the decay occurs via d- or f-wave neutron emission. As such, the spin and parity of the ^{27}O resonance may be tentatively assigned to be $3/2^+$ or $7/2^-$.

Momentum distribution Extended Data Fig. 4 shows the transverse momentum (P_x) distribution of the ^{24}O+3n system in the rest frame of the ^{29}F beam for events gated by $E_{012} < 0.08$ MeV and $E_{0123} < 0.8$ MeV – that is, events corresponding to population of the ^{28}O ground state. We note that this analysis employed the ^{24}O+3n events as the limited ^{24}O+4n statistics could not be usefully exploited in distinguishing between the momentum distributions for the proton knockout from different orbitals. Even though the momentum distribution is slightly broadened by the undetected decay neutron, it still reflects directly the character of the knocked-out proton.

The experimental P_x distribution is compared to DWIA (Distorted Wave Impulse Approximation) reaction theory calculations (see below) for knockout of a proton from the $1d_{5/2}$ and $2s_{1/2}$ orbitals. The theoretical distributions are convoluted with the experimental resolution as well as the much smaller broadening induced by the undetected neutron ($\sigma =$ 34 MeV/c). The best fit normalization of the theoretical distribution obtained by the distorting potential with the Dirac phenomenology (microscopic folding model potential) through a χ^2 minimization gives reduced-χ^2 values of 2.0 (2.0) for the $1d_{5/2}$ proton knockout and 3.7 (4.7) for the $2s_{1/2}$ knockout. The curves in Extended Data Fig. 4 represent the calculations obtained by the distorting potential with the Dirac phenomenology. The better agreement for the $1d_{5/2}$ proton knockout suggests that the spin and parity of the ^{29}F ground state is $5/2^+$ as predicted by the shell model calculations, including those using the EEdf3 interaction.

EEdf3 calculations The EEdf3 Hamiltonian[32] is a variant of the EEdf1 Hamiltonian, which was used in ref.[33] for describing F, Ne, Na, and Mg isotopes up to neutron dripline[32]. The EEdf1 Hamiltonian was derived from chiral effective field theory (χEFT) interaction, as described below. The χEFT interaction proposed by Entem and Machleidt[62,63] was taken with $\Lambda = 500$ MeV, as the nuclear force in vacuum, up to the next-to-next-to-next-to-leading-order (N^{3}LO) in the χEFT. It was then renormalized using the $V_{low\text{-}k}$ approach[64,65] with a cutoff of $\Lambda_{V_{low\text{-}k}} = 2.0$ fm^{-1}, in order to obtain a low-momentum interaction decoupled from high-momentum phenomena. The EKK method[66–68] was then adopted in order to obtain the effective NN interaction for the sd-pf shells, by including the so-called $\hat{Q}$-box, which incorporates unfolded effects coming from outside of the model space[69], up to third order and its folded diagrams. As to the single-particle basis vectors, the eigenfunctions of the three-dimensional harmonic oscillator potential were taken as usual. In addition, the contributions from the Fujita Miyazawa three-nucleon force (3NF)[70] were added in the form of the effective NN interaction[41]. The Fujita Miyazawa force represents the effects of the virtual excitation of a nucleon to a Δ baryon by pion-exchange processes and includes the effects of Δ-hole excitations, but does not include other effects such as contact (c_D and c_E) terms.

In the present study, we explicitly treat neutrons only, while the protons remained confined to the ^{16}O closed-shell core. As such, there is no proton-neutron interaction between active nucleons, and the neutron-neutron interaction is weaker. As this increases the relative importance of the effects from 3NF, we adopt the more modern 3NF of Hebeler et al.[44], which is expected to have finer details and improved properties. We obtain effective NN interactions from this 3NF first by deriving density-dependent NN interactions from them[71] and then by having the density dependence integrated out with the normal density. It was suggested that this 3NF produces results similar to those reported in ref.[33] for the F, Ne, Na and Mg isotopes. As a result of this change, the single-particle energies are shifted for the $1d_{5/2}$ and $2s_{1/2}$ orbitals by -0.72 MeV, for the $1d_{3/2}$ orbital by -0.42 MeV and for the pf shell orbitals by 0.78 MeV.

Coupled-cluster calculations and emulators The starting point for the calculations is the intrinsic Hamiltonian,

$$H = T_{\text{kin}} - T_{\text{CoM}} + V_{NN} + V_{NNN}. \tag{1}$$

Here T_{kin} is the kinetic energy, T_{CoM} the kinetic energy of the center-of-mass, and $V_{NN} + V_{NNN}$ are nucleon-nucleon and three-nucleon potentials from χEFT[62,72,73] and include Delta isobars[74]. The momentum space cutoff of this interaction is $\Lambda = 394$ MeV/c.

We used the coupled-cluster method[75–81] with singles-doubles and perturbative triples excitations, known as the CCSDT-3 approximation[82,83], to compute the ground-state energy of ^{28}O, and the particle-removed equation-of-motion (EOM) coupled-cluster method from refs.[84],[85] for the ground-state energy of ^{27}O. The coupled-cluster calculations start from a spherical Hartree-Fock reference of ^{28}O in a model-space of 13 major harmonic oscillator shells with an oscillator frequency of $\hbar\omega = 16$ MeV. The three-nucleon force is limited to three-body energies up to $E_{3\text{max}} = 14\hbar\omega$. For energy differences the effects of model-space truncations and coupling to the scattering continuum are small and were neglected in the history matching analysis.

The low-energy constants (LECs) of this interaction are constrained by a history matching approach employing high-precision emulators enabled by eigenvector continuation[86]. These tools mimic the results of actual coupled-cluster computations, but are several orders of magnitude faster to evaluate, hence facilitating comprehensive exploration of the relevant parameter space. The emulators work as follows. In the 17-dimensional space of LECs, the parameterization of the $\Delta\mathrm{NNLO}_{\mathrm{GO}}(394)$ potential[74] serves as a starting point around which we select emulator training points according to a space-filling lattice hypercube design for which we perform coupled-cluster computations of ground-state energies, radii, and excited states of $^{16,22,24}\mathrm{O}$ (see Extended Data Table **1** for details). Keeping track of the variations of the observables and the corresponding coupled-cluster eigenstates as the low-energy constants are varied, allows us to construct an emulator that can be used to predict the results for novel parameterizations. This emulator strategy is rather general[87] and possible because the eigenvector trajectory generated by continuous changes of the low-energy constants only explores a relatively small subspace of Hilbert space. Eigenvector continuation emulation tailored to coupled-cluster eigenstates is referred to as the subspace-projected coupled-cluster (SP-CC) method. In this work, we extended the SP-CC method of ref.[88] to excited states and increased the precision by including triples excitations via the CCSDT-3 and EOM-CCSDT-3 methods, respectively. Our SP-CC emulators employ up to 68 training points for each observable of interest, and use model spaces consisting of 11 major harmonic oscillator shells. We checked the precision of each emulator by performing emulator diagnostics[89]: confronting the emulator predictions with the results of actual coupled-cluster computations, see Extended Data Fig. 5. Once constructed, the emulators are inexpensive computational tools that can precisely predict the results for virtually arbitrary parameterizations of the EFT potentials. This allows us to explore several hundred million parameterizations with the computational cost of only a few hundred actual coupled-cluster computations. The use of emulation hence represents a critical advance, that facilitates a far deeper analysis of the coupled-cluster method, that was previously infeasible due to the substantial computational expense of the coupled-cluster calculations. Hence, these techniques overcome a major barrier to the use of such coupled-cluster methods.

Coupled-cluster calculations: Linking models to reality We describe the relationship between experimental observations, z, and *ab inito* model predictions $M(\theta)$, where θ denotes the parameter vector of the theoretical model, as

$$z = M(\theta) + \epsilon_{\mathrm{method}} + \epsilon_{\mathrm{model}} + \epsilon_{\mathrm{exp}}. \tag{2}$$

In this relation, we consider experimental uncertainties, ϵ_{exp}, as well as method approximation errors $\epsilon_{\mathrm{method}}$. The latter represent, e.g., model-space truncations and other approximations in the *ab initio* many-body solvers and are estimated from method convergence studies[74]. Most importantly, we acknowledge the fact that even if we were to evaluate the model $M(\theta)$ at its best possible choice of the parameter vector, θ^*, the model output, $M(\theta^*)$, would still not be in exact quantitative agreement with reality due to, e.g., simplifications and approximations inherent to the model. We describe this difference in terms of a model discrepancy term, $\epsilon_{\mathrm{model}}$. The expected EFT-convergence pattern of our model allows us to specify further probabilistic attributes of $\epsilon_{\mathrm{model}}$ a priori[90–93]. We employ the model errors defined in[94]. The use of emulators based on eigenvector continuation[86–88] provides us with an efficient approximation, $\tilde{M}(\theta)$, of the model. This approach entails an emulator error $\epsilon_{\mathrm{emulator}}$ such that $M(\theta) = \tilde{M}(\theta) + \epsilon_{\mathrm{emulator}}$, as outlined in the previous section.

Obviously, we do not know the exact values of the errors in Eq. (2), hence we represent them as uncertain quantities and specify reasonable forms for their statistical distributions, in alignment with the Bayesian paradigm. This allows for these uncertainties to be formally incorporated in all subsequent calculations and inferences. We also assume that the errors add independently of each other and the inputs θ.

Coupled-cluster calculations: History matching In this work we use an iterative approach for complex computer models known as history matching (HM)[45–47] in which the model, solved at different fidelities, is confronted with experimental data z using relation (2). The aim of HM is to estimate the set $\mathcal{Q}(z)$ of values for θ, for which the evaluation of a model $M(\theta)$ yields an acceptable—or at least not implausible (NI)—match to a set of observations z. HM has been employed in various studies[95–97] ranging, e.g., from effects of climate modeling[98,99] to systems biology[47]. The present work represents the first application in nuclear physics. We introduce the standard implausibility measure

$$I^2(\theta) = \max_{i\in\mathcal{Z}} \frac{|\tilde{M}_i(\theta) - z_i|^2}{\mathrm{Var}\left(\tilde{M}_i(\theta) - z_i\right)}, \tag{3}$$

which is a function over the input parameter space and quantifies the (mis-)match between our (emulated) model output $\tilde{M}_i(\theta)$ and the observation z_i for all observables i in the target set $\mathcal{Z}$. This specific definition uses the maximum of the individual implausibility measures (one for each observable) as the restricting quantity. We consider a particular value for θ as implausible if $I(\theta) > c_I \equiv 3.0$ appealing to Pukelsheim's three-sigma rule[100]. In accordance with the assumptions leading to Eq. (2), the variance in the denominator of Eq. (3) is a sum of independent squared errors. Generalizations of these assumptions are straightforward if additional information on error covariances or possible inaccuracies in our error model would become available. An important strength of the HM approach is that we can proceed iteratively, excluding regions of input space by imposing cutoffs on implausibility measures that can include *additional* observables z_i and corresponding model outputs M_i, and possibly refined emulators $\tilde{M}_i$, as the iterations proceed. The iterative HM proceeds in waves according to a straightforward strategy that can be summarized as follows:

1. At iteration j: Evaluate a set of model runs over the current NI volume $\mathcal{Q}_j$ using a space-filling design of sample values for the parameter inputs θ. Choose a rejection strategy based on implausibility measures for a set $\mathcal{Z}_j$ of informative observables.

2. Construct or refine emulators for the model predictions across the current non-implausible volume $\mathcal{Q}_j$.

3. The implausibility measures are then calculated over $\mathcal{Q}_j$, using the emulators, and implausibility cutoffs are imposed. This defines a new, smaller NI volume $\mathcal{Q}_{j+1}$ which should satisfy $\mathcal{Q}_{j+1} \subset \mathcal{Q}_j$.

4. Unless (a) the emulator uncertainties for all observables of interest are sufficiently small in comparison to the other sources of uncertainty, (b) computational resources are exhausted, or (c) all considered points in the parameter space are deemed implausible, we:
    - include any additional informative observables in the considered set $\mathcal{Z}_{j+1}$, and return to step 1.
5. If 4(a) or (b) is true we generate a large number of acceptable runs from the final NI volume Q_{final}, sampled according to scientific need.

The *ab initio* model for the observables we consider comprises at most 17 parameters; 4 subleading pion-nucleon couplings, 11 nucleon-nucleon contact couplings, and 2 short-ranged three-nucleon couplings. To identify a set of NI parameter samples we performed iterative HM in four waves using observables and implausibility measures as summarized in Extended Data Table **1**. For each wave we employ a sufficiently dense latin hypercube set of several million candidate parameter samples. For the model evaluations we utilized fast computations of neutron-proton (*np*) scattering phase shifts and efficient emulators for the few- and many-body observables listed. See Extended Data Table **2** for the list of included observables and key information for each wave. The input volume for wave 1 included large ranges for the relevant parameters, as indicated by the panel ranges in the lower left triangle of Extended Data Fig. 6. In all four waves, the input volume for $c_{1,2,3,4}$ is a four-dimensional hypercube mapped onto the multivariate Gaussian pdf resulting from a Roy-Steiner analysis of πN scattering data[101]. In wave 1 and wave 2 we sampled all relevant parameter directions for the set of included two-nucleon observables. In wave 3, the additional ^{3}H and ^{4}He observables were added. Since they are known to be rather insensitive to the four model parameters acting solely in the $P-$wave, we therefore ignored this subset of the inputs and compensated by slightly enlarging the corresponding method errors. This is a well-known emulation procedure called inactive parameter identification[45]. For the final iteration, i.e. wave 4, we considered all 17 model parameters and added a set of observables for the oxygen isotopes ^{16,22,24}O and emulated the model outputs for 5×10^8 parameter samples. Extended Data Fig. 6 summarizes the sequential NI volume reduction, wave-by-wave, and indicates the set Q_4 of 634 NI samples after the fourth and final wave. The volume reduction is guided by the implausibility measure (3) and the optical depths (see Eqs. (25) and (26) in ref.[47]), where the latter are illustrated in the lower left triangle of Extended Data Fig. 6. The NI samples summarise the parameter region of interest, and can directly aid insight regarding interdependencies between parameters induced by the match to observed data. This region is also where we would expect the posterior distribution to reside. We see that the iterative history matching process trains a nested series of emulators that become more and more accurate over this posterior region, as the iterations progress.

Coupled-cluster calculations: Bayesian posterior sampling The NI samples in the final HM wave also serve as excellent starting points for extracting the posterior probability density function (pdf) of the parameters θ, i.e. $p(\theta|A = 2-24)$. To this end, we assume a normally distributed likelihood, according to Eq. (2), and a uniform prior corresponding to the initial volume of wave 1. Note that the prior for $c_{1,2,3,4}$ is the multivariate Gaussian resulting from a Roy-Steiner analysis of πN scattering data[101]. We sample the posterior using the affine invariant Markov Chain Monte Carlo ensemble sampler emcee[102] and the resulting distribution is shown in the upper right triangle of Extended Data Fig. 6. The sampling was performed with four independent ensemble chains, each with 150 walkers, and satisfactory convergence was reached (diagnosed using the Gelman-Rubin test with $|\hat{R} - 1| < 10^{-4}$ in all dimensions). We performed $5 \cdot 10^5$ iterations per walker—after an initial warm-up of 5000 steps—and kept one final sample for every 500 steps. Combining all chains we therefore end up with $4 \times 150 \times 1000 = 6 \cdot 10^5$ final samples. In addition, we explored the sensitivity of our results to modifications of the likelihood definition. Specifically, we used a student-t distribution ($\nu = 5$) to see the effects of allowing heavier tails, and we introduced an error covariance matrix to study the effect of correlations ($\rho \approx 0.6$) between selected observables. In the end, the differences in the extracted credibility regions was not great and we therefore present only results obtained with the uncorrelated, multivariate normal distribution (see Extended Data Table **3**).

A subset of marginal posterior predictive distributions (ppd) are shown in Extended Data Fig. 7. Clearly, a subset of 100 samples provides an accurate low-statistics representation of this marginalized ppd. We exploit this feature in our final predictions for ^{27,28}O presented in the main text. Note that the ppd does not include draws from the model discrepancy pdf. To include information about the ^{25}O separation energy with respect to ^{24}O we perform a straightforward Bayesian update of the posterior pdf $p(\theta|A = 2-24)$ for the LECs. This complements the statistical analysis of the *ab initio* model with important information content from an odd and neutron-rich oxygen isotope. Using the pdf $p(\theta|A = 2-24)$ we draw 500 model predictions for $\Delta E(^{25,24}\text{O})$ and account for all independent and normally distributed uncertainties according to Extended Data Table **1**. Next, we draw 121 different LEC parameterizations from the updated posterior and use coupled cluster to compute the corresponding ground-state energies of ^{27,28}O. The full bivariate ppd for the ^{28}O–^{24}O and ^{27}O–^{28}O energy differences, $\Delta E(^{28,24}\text{O})$ and $\Delta E(^{27,28}\text{O})$, with associated credible regions, are shown in Extended Data Fig. 3. The effect of the continuum on the energy difference was estimated to be ~0.5 MeV in ref.[39] and was neglected in this work. We note that our ability to examine the full ppd for these expensive *ab initio* calculations provides welcome additional insight, which is a direct consequence of the use of the HM procedure. We note that a sufficiently precise determination of $\Delta E(^{28,24}\text{O})$ and $\Delta E(^{27,28}\text{O})$ requires wave 4 in the history matching and also using the separation energy $\Delta E(^{24,25}\text{O})$ for the construction of the pdf. Without input about ^{25}O, the separation energy $\Delta E(^{27,28}\text{O})$ becomes too uncertain to be useful. It is in this sense that a sufficiently precise prediction of $\Delta E(^{27,28}\text{O})$ is finely tuned and cannot be based only on the properties of light nuclei up to ^{4}He. Changes in the low-energy constants that have small impact in few nucleon systems are magnified in ^{28}O. Apparently, one needs information about all nuclear shells including the *sd* shell to meaningfully predict this key nucleus.

DWIA calculations The distorted-wave impulse approximation (DWIA)[53 103,104] describes proton-induced proton knockout – $(p, 2p)$ – processes as proton-proton (*pp*) elastic scattering. This is referred to as the impulse approximation, which is considered to be valid at intermediate energies when both outgoing protons have large momenta with respect to the residual nucleus. The DWIA approach has been successful in describing proton-induced knockout reactions; in ref.[53], it was shown that the spectroscopic factors deduced from $(p,2p)$ reactions for the single-particle levels near the Fermi surface of several nuclei are consistent with those extracted from electron-induced $(e,e'p)$ reactions. The transition matrix of $(p,2p)$ processes within DWIA theory is given by $T_{p2p} = \left\langle \chi_1\chi_2 \left| t_{pp} \right| \chi_0\phi_p \right\rangle$, where χ_i are the distorted waves of the incoming proton (0) and the outgoing two protons (1 and 2), whereas ϕ_p is the normalized bound-state wave function of the proton inside the nucleus. The pp effective interaction is denoted by t_{pp}, the absolute square of which is proportional to the pp elastic cross section. The nonlocality corrections[105] to both χ_i and ϕ_p are taken into account as well as the Moller factor[106] for t_{pp} that guarantees the Lorentz invariance of the pp reaction probability. The $(p,2p)$ cross section is given by $F_{\mathrm{kin}} C^2 S \left| T_{p2p} \right|^2$ with F_{kin} being a kinetic factor and $C^2 S$ the spectroscopic factor.

In this study, the cross section integrated over the allowed kinematics of the outgoing particles was calculated. We employed the Franey-Love parameterization[107] for t_{pp} and the Bohr-Mottelson's (BM) single-particle potential[108] in order to compute ϕ_p. We have used two types of the one-body distorting potential to obtain χ – specifically, the Dirac phenomenology (set EDAD2[109]) and a microscopic folding model potential based on the Melbourne G-matrix interaction[110] and one-body nuclear densities calculated with the BM single-particle model[108]. It was found that the difference in the $(p,2p)$ cross sections calculated with the two sets of distorting potentials was at most 7.5%. In addition, they give almost identical shapes for the momentum distributions. As such, we have adopted here the average value of the cross sections for each single-particle configuration.

Data availability Source data for Figs. 2a-c, Extended Data Figs. 2a-f, and Extended Data Fig. 4 are provided with this paper. All of the other relevant data that support the findings of this study are available from the corresponding author upon reasonable request.

Code availability Our unpublished computer codes used to generate the results reported in this paper are available from the corresponding author upon reasonable request.

References

55. Kubo, T. *et al.* BigRIPS separator and ZeroDegree spectrometer at RIKEN RI Beam Factory. Prog. Theor. Exp. Phys. **2012**, 03C003 (2012).
56. Agostinelli, S. *et al.* GEANT4—a simulation toolkit. Nucl. Instrum. Methods Phys. Res. Sect. A **506**, 250–303 (2003).
57. Nakamura, T. & Kondo, Y. Large acceptance spectrometers for invariant mass spectroscopy of exotic nuclei and future developments. Nucl. Instrum. Methods Phys. Res., Sect. B **376**, 156–161 (2016).
58. Kondo, Y., Tomai, T. & Nakamura, T. Recent progress and developments for experimental studies with the SAMURAI spectrometer. Nucl. Instrum. Methods Phys. Res., Sect. B **463**, 173–178 (2020).
59. Grigorenko, L. V., Mukha, I. G., Scheidenberger, C. & Zhukov, M. V. Two-neutron radioactivity and four-nucleon emission from exotic nuclei. Phys. Rev. C **84**, 021303 (2011).
60. Lane, A. M. & Thomas, R. G. R-Matrix Theory of Nuclear Reactions. Rev. Mod. Phys. **30**, 257–353 (1958).
61. Dover, C. B., Mahaux, C. & Weidenmüller, H. A. The single-particle limit for partial widths. Nucl. Phys. A **139**, 593–604 (1969).
62. Machleidt, R. & Entem, D. Chiral effective field theory and nuclear forces. Phys. Rep. **503**, 1–75 (2011).
63. Entem, D. R. & Machleidt, R. Accurate charge-dependent nucleon-nucleon potential at fourth order of chiral perturbation theory. Phys. Rev. C **68**, 041001 (2003).
64. Bogner, S., Kuo, T. T. S., Coraggio, L., Covello, A. & Itaco, N. Low momentum nucleon-nucleon potential and shell model effective interactions. Phys. Rev. C **65**, 051301 (2002).
65. Nogga, A., Bogner, S. K. & Schwenk, A. Low-momentum interaction in few-nucleon systems. Phys. Rev. C **70**, 061002 (2004).
66. Takayanagi, K. Effective interaction in non-degenerate model space. Nucl. Phys. A **852**, 61–81 (2011).
67. Takayanagi, K. Effective Hamiltonian in the extended Krenciglowa-Kuo method. Nucl. Phys. A **864**, 91–112 (2011).
68. Tsunoda, N., Takayanagi, K., Hjorth-Jensen, M. & Otsuka, T. Multi-shell effective interactions. Phys. Rev. C **89**, 024313 (2014).
69. Hjorth-Jensen, M., Kuo, T. T. & Osnes, E. Realistic effective interactions for nuclear systems. Phys. Rep. **261**, 125–270 (1995).
70. Fujita, J. & Miyazawa, H. Pion theory of three-body forces. Prog. Theor. Phys. **17**, 360 (1957).
71. Kohno, M. Nuclear and neutron matter G-matrix calculations with a chiral effective field theory potential including effects of three-nucleon interactions. Phys. Rev. C **88**, 064005 (2013). ; erratum **96**, 059903 (2017).
72. van Kolck, U. Few-nucleon forces from chiral Lagrangians. Phys. Rev. C **49**, 2932–2941 (1994).
73. Epelbaum, E., Hammer, H.-W. & Meißner, U.-G. Modern theory of nuclear forces. Rev. Mod. Phys. **81**, 1773–1825 (2009).
74. Jiang, W. G. *et al.* Accurate bulk properties of nuclei from $A = 2$ to ∞ from potentials with Δ isobars. Phys. Rev. C **102**, 054301 (2020).
75. Coester, F. Bound states of a many-particle system. Nucl. Phys. **7**, 421–424 (1958).
76. Coester, F. & Kümmel, H. Short-range correlations in nuclear wave functions. Nucl. Phys. **17**, 477–485 (1960).
77. Kümmel, H., Lührmann, K. H. & Zabolitzky, J. G. Many-fermion theory in expS- (or coupled cluster) form. Phys. Rep. **36**, 1–63 (1978).
78. Mihaila, B. & Heisenberg, J. H. Microscopic Calculation of the Inclusive Electron Scattering Structure Function in ^{16}O. Phys. Rev. Lett. **84**, 1403–1406 (2000).
79. Dean, D. J. & Hjorth-Jensen, M. Coupled-cluster approach to nuclear physics. Phys. Rev. C **69**, 054320 (2004).
80. Bartlett, R. J. & Musiał, M. Coupled-cluster theory in quantum chemistry. Rev. Mod. Phys. **79**, 291–352 (2007).
81. Hagen, G., Papenbrock, T., Hjorth-Jensen, M. & Dean, D. J. Coupled-cluster computations of atomic nuclei. Rep. Prog. Phys. **77**, 096302 (2014).
82. Noga, J., Bartlett, R. J. & Urban, M. Towards a full CCSDT model for electron correlation. CCSDT-n models. Chem. Phys. Lett. **134**, 126–132 (1987).
83. Watts, J. D. & Bartlett, R. J. Iterative and non-iterative triple excitation corrections in coupled-cluster methods for excited electronic states: the EOM-CCSDT-3 and EOM-CCSD($\tilde{T}$) methods. Chem. Phys. Lett. **258**, 581–588 (1996).
84. Gour, J. R., Piecuch, P., Hjorth-Jensen, M., Włoch, M. & Dean, D. J. Coupled-cluster calculations for valence systems around ^{16}O. Phys. Rev. C **74**, 024310 (2006).
85. Morris, T. D. *et al.* Structure of the Lightest Tin Isotopes. Phys. Rev. Lett. **120**, 152503 (2018).
86. Frame, D. *et al.* Eigenvector Continuation with Subspace Learning. Phys. Rev. Lett. **121**, 032501 (2018).

87. König, S., Ekström, A., Hebeler, K., Lee, D. & Schwenk, A. Eigenvector continuation as an efficient and accurate emulator for uncertainty quantification. Phys. Lett. B **810**, 135814 (2020).
88. Ekström, A. & Hagen, G. Global Sensitivity Analysis of Bulk Properties of an Atomic Nucleus. Phys. Rev. Lett. **123**, 252501 (2019).
89. Bastos, L. S. & O′Hagan, A. Diagnostics for Gaussian Process Emulators. Technometrics **51**, 425–438 (2009).
90. Wesolowski, S., Klco, N., Furnstahl, R., Phillips, D. & Thapaliya, A. Bayesian parameter estimation for effective field theories. J. Phys. G **43**, 074001 (2016).
91. Melendez, J., Wesolowski, S. & Furnstahl, R. Bayesian truncation errors in chiral effective field theory: nucleon-nucleon observables. Phys. Rev. C **96**, 024003 (2017).
92. Wesolowski, S., Furnstahl, R., Melendez, J. & Phillips, D. Exploring Bayesian parameter estimation for chiral effective field theory using nucleon–nucleon phase shifts. J. Phys. G **46**, 045102 (2019).
93. Melendez, J., Furnstahl, R., Phillips, D., Pratola, M. & Wesolowski, S. Quantifying Correlated Truncation Errors in Effective Field Theory. Phys. Rev. C **100**, 044001 (2019).
94. Ekström, A., Hagen, G., Morris, T. D., Papenbrock, T. & Schwartz, P. D. Δ isobars and nuclear saturation. Phys. Rev. C **97**, 024332 (2018).
95. Raftery, A. E., Givens, G. H. & Zeh, J. E. Inference from a Deterministic Population Dynamics Model for Bowhead Whales. J. Am. Stat. Assoc. **90**, 402–416 (1995).
96. Vernon, I., Goldstein, M. & Bower, R. G. Rejoinder. Bayesian Anal. **5**, 697–708 (2010).
97. Andrianakis, I. *et al.* Bayesian history matching of complex infectious disease models using emulation: a tutorial and a case study on HIV in Uganda. PLoS Comput Biol. **11**, e1003968 (2015).
98. Williamson, D. *et al.* History matching for exploring and reducing climate model parameter space using observations and a large perturbed physics ensemble. Clim. Dyn. **41**, 1703 (2013).
99. Edwards, T. L. *et al.* Revisiting Antarctic ice loss due to marine ice-cliff instability. Nature **566**, 58–64 (2019).
100. Pukelsheim, F. The Three Sigma Rule. The American Statistician **48**, 88–91 (1994).
101. Siemens, D. *et al.* Reconciling threshold and subthreshold expansions for pion-nucleon scattering. Phys. Lett. B **770**, 27–34 (2017).
102. Foreman-Mackey, D., Hogg, D. W., Lang, D. & Goodman, J. emcee: The MCMC Hammer. Publications of the Astronomical Society of the Pacific **125**, 306–312 (2013).
103. Jacob, G. & Maris, T. A. J. Quasi-free scattering and nuclear structure. Rev. Mod. Phys. **38**, 121–142 (1966).
104. Jacob, G. & Maris, T. A. J. Quasi-free scattering and nuclear structure. II. Rev. Mod. Phys. **45**, 6–21 (1973).
105. Perey, F. & Buck, B. A non-local potential model for the scattering of neutrons by nuclei. Nucl. Phys. **32**, 353–380 (1962).
106. Møller, C. General properties of the characteristic matrix in the theory of elementary particles. Kgl. Danske Videnskab. Selskab, Mat-fys. Medd. , 1 (1945).
107. Franey, M. A. & Love, W. G. Nucleon-nucleon t-matrix interaction for scattering at intermediate energies. Phys. Rev. C **31**, 488–498 (1985).
108. Bohr, A. & Mottelson, B. R. NUCLEAR STRUCTURE. Vol. I (Benjamin, 1969).
109. Cooper, E. D., Hama, S., Clark, B. C. & Mercer, R. L. Global Dirac phenomenology for proton-nucleus elastic scattering. Phys. Rev. C **47**, 297–311 (1993).
110. Amos, K., Dortmans, P., von Geramb, H., Karataglidis, S. & Raynal, J. ADVANCES IN NUCLEAR PHYSICS. edited by J.W. Negele and E. Vogt, (Plenum, New York 2000).

Acknowledgement We thank the RIKEN Nishina Center and the Center for Nuclear Study, the University of Tokyo accelerator staff for the excellent beam delivery. This work was supported in part by JSPS KAKENHI Grants No. 18K03672. and No. 18H05404. This work was also supported by the Deutsche Forschungsgemeinschaft (DFG, German Research Foundation) - Proj.- ID 279384907 - SFB 1245, the GSI-TU Darmstadt cooperation agreement, the GSI under contract KZILGE1416, the German Federal Ministry for Education and Research (BMBF) under contract No. 05P15RDFN1 and 05P21PKFN1, the European Research Council (ERC) under the European Union's Horizon 2020 research and innovation programme (grant agreement numbers 758027 and 258567), the Swedish Research Council grant number 2011-5324, 2017-03839 and 2017-04234. Partial support was also supplied by the Franco-Japanese LIA-International Associated Laboratory for Nuclear Structure Problems as well as the French ANR-14-CE33-0022-02 EXPAND. This work was also supported in part by the Institute for Basic Science (IBS-R031-D1) in Korea and the U.S. Department of Energy, Office of Science, Office of Nuclear Physics, under Award Nos. DE-FG02-96ER40963 and DE-SC0018223. This work was also supported in part by the National Science Foundation, USA under Grant No. PHY-1102511. Computer time was provided by the Innovative and Novel Computational Impact on Theory and Experiment (INCITE) program. This research employed resources of the Oak Ridge Leadership Computing Facility at the Oak Ridge National Laboratory, which is supported by the Office of Science of the U.S. Department of Energy under Contract No. DE-AC05-00OR22725, and resources provided by the Swedish National Infrastructure for Computing (SNIC) at Chalmers Centre for Computational Science and Engineering (C3SE), and the National Supercomputer Centre (NSC) partially funded by the Swedish Research Council. Y.T. acknowledges the support of the JSPS Grant-in-Aid for Scientific Research Grants No. JP21H01114. I.G. has been supported by HIC for FAIR and Croatian Science Foundation under projects no. 1257 and 7194. Z.D. and D.S. have been supported by the National Research, Development and Innovation Fund of Hungary via project No. TKP2021-NKTA-42 and K128947. T.O., N.S., N.T., Y.U., and S.Y. acknowledge valuable support from the "Priority Issue on post-K computer" (hp190160), "Program for Promoting Researches on the Supercomputer Fugaku" (JPMXP1020200105,hp200130,hp210165), and the KAKENHI Grants (17K05433, 20K03981, JP19H05145, JP21H00117). The material presented here is based upon work supported in part by the U.S. Department of Energy, Office of Science, Office of Nuclear Physics, under Contract No. DE-AC02-06CH11357 (ANL).

Author Contributions Y.K. designed and proposed the experiment, performed the offline analysis and the Monte Carlo simulations. Y.K., T.N., T.O., K.O., and N.A.O. drafted the manuscript. Y.K., T.N., N.L.A, H.F., L.A., T.A., H.B., K.B., C.C., D.C., H.C., N.C., A.C., F.D., A.D., Q.D., Z.D., C.A.D., Z.E., I.G., J.-M.G., J.G., A.G., M.N.H., A.H., C.R.H., M.H., A.H., Á.H., J.W.H., T.I., J.K., N.K-N., S.K., S.K., K.K., T.K., D.K., S.K., I.K., V.L., S.L., F.M.M., S.M., J.M., K.M., T.M., M.N., K.N., N.N., T.N., A.O., F.O.S., N.A.O., H.O., T.O., V.P., S.P., A.R., D.R., A.T.S., T.S., M.S., H.S., Y.S., H.S., F.S., P.S., M.S., Y.S., H.S., D.S., O.S., L.S., S.T., M.T., M.T., H.T., Y.T., T.T., J.T., J.T., T.U., H.W., Z.Y., M.Y., and K.Y. took part in the setting up of the experiment and/or monitored the data accumulation and/or maintained the operation of experiment and detectors. T.O., N.S., N.T., Y.U. and S.Y. performed the EEdf3 calculations. K.O. performed the DWIA calculations. A.E., C.F., G.H., W.G.J., T.P., Z.H.S., and I.V. performed the coupled-cluster calculations and their statistical analysis and wrote the associated sections of the manuscript.

Competing Interests The authors declare no competing interests.

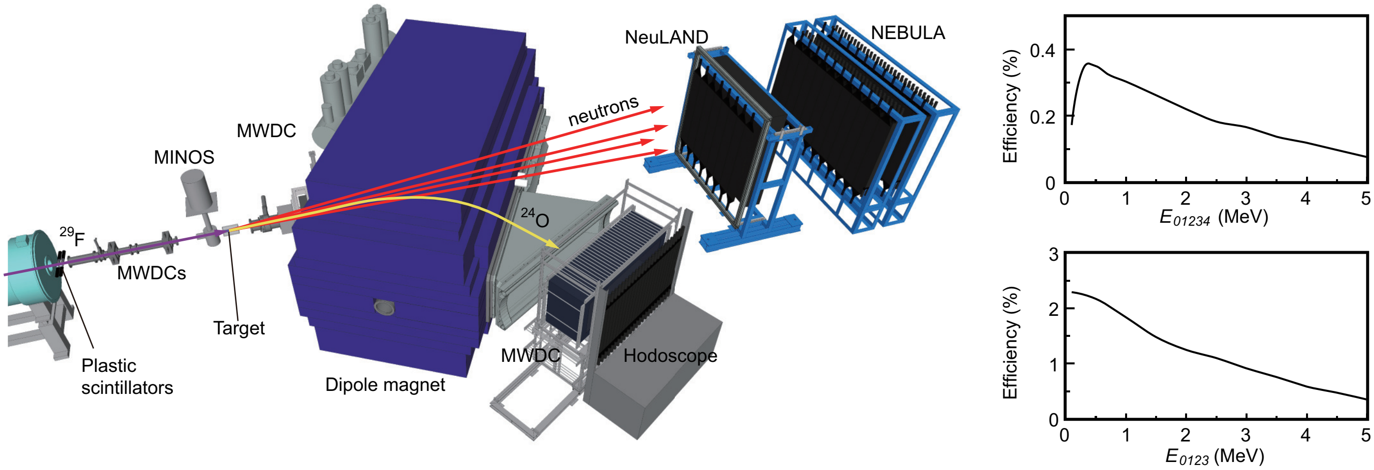

Extended Data Fig. 1 | Schematic view of the experimental setup. The insets show the overall efficiency as a function of decay energy for detecting ^{24}O + 3 and 4 neutrons.

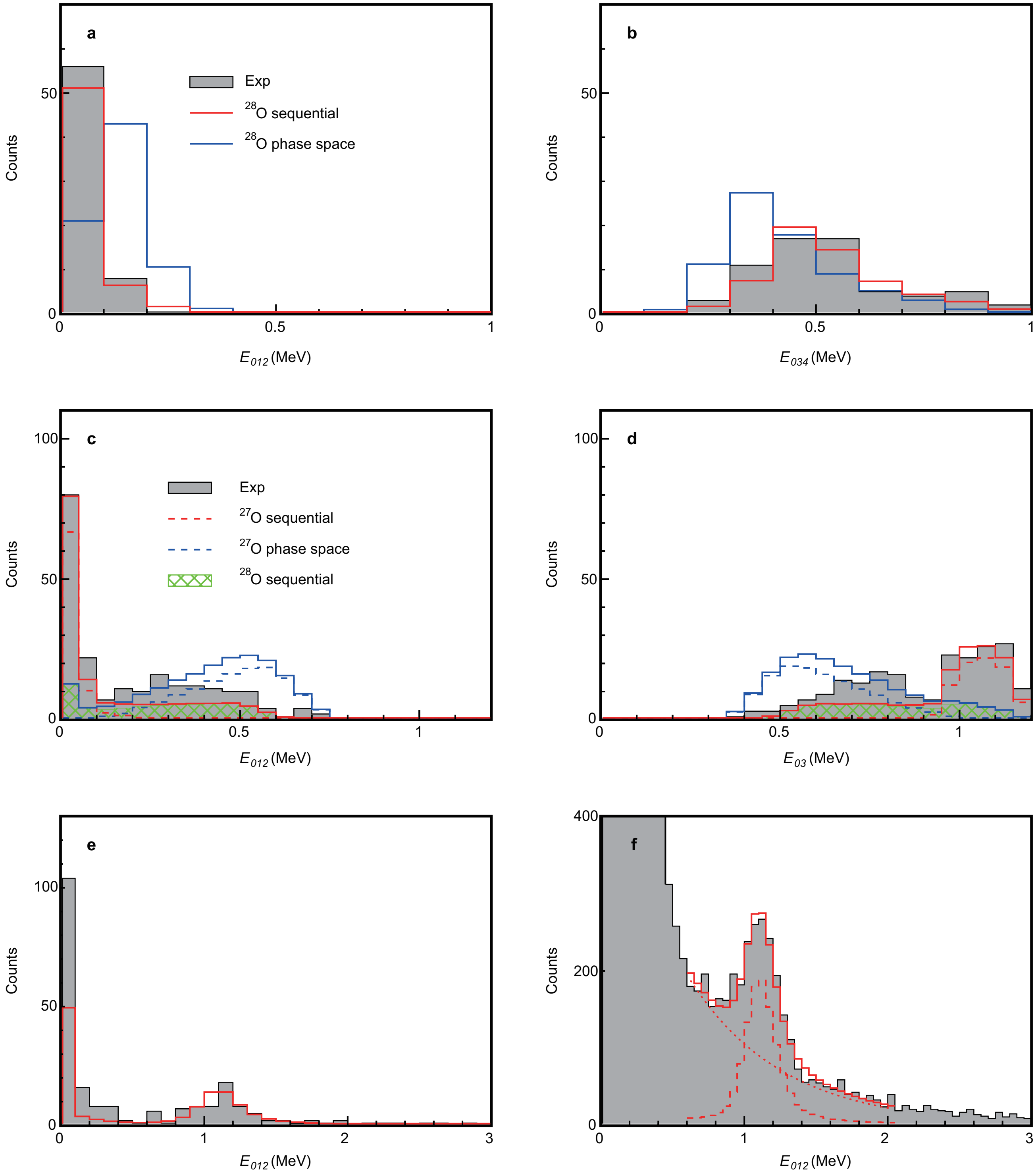

Extended Data Fig. 2 | Partial decay energy spectra. a, The filled grey histogram is the three-body decay energy E_{012} gated on the total decay energy $E_{01234} < 1$ MeV for the ^{24}O+4n coincidence events. The red and blue histograms are the results of simulations of sequential decay via the ^{26}O ground state (A and B in Fig. 2e) and five-body phase space decay, respectively. **b**, Same as a, but for the three-body decay energy E_{034}. **c**, The filled grey histogram is the partial decay energy spectrum E_{012} gated by $1.0 < E_{0123} < 1.2$ MeV for the ^{24}O+3n coincidence events. The red and blue dashed histograms are the results of simulations assuming ^{27}O sequential (B and C in Fig. 2e) and four-body phase space decay, respectively. The green hatched histogram represents the contribution from the decay of ^{28}O. The red (blue) solid histogram is the sum of the contributions from ^{28}O and ^{27}O for sequential (phase space) decay. **d**, Same as c, but for the two-body decay energy E_{03}. **e**, Decay energy spectrum of ^{24}O+2n events from the ^{29}Ne beam data. The grey histogram represents events with $E_{01} < 0.08$ MeV. The red histogram shows the results of the simulation for the decay of the ^{27}O resonance. The excess observed near zero decay energy is interpreted as arising from direct population of the ^{26}O ground state from ^{29}Ne. **f**, Decay energy spectrum of ^{24}O+2n events from the ^{29}F beam. The grey histogram represents events with $E_{01} < 0.08$ MeV. The red histogram shows the best fit in the region of the peak arising from the decay of the ^{27}O resonance (dashed histogram) and an exponential distribution (dotted curve) arising from all other contributions which come primarily from the decay of ^{28}O.

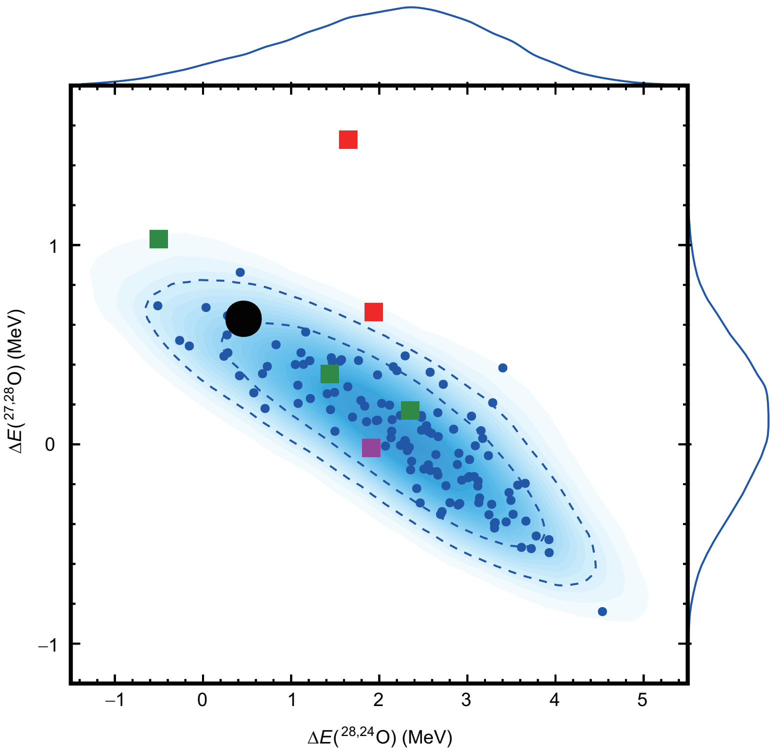

Extended Data Fig. 3 | Probability distribution of the calculated energy differences. Survived non-implausible calculations are shown by blue dots as functions of energy differences $\Delta E(^{28,24}\mathrm{O})$ and $\Delta E(^{27,28}\mathrm{O})$. The black circle shows experiment. The dashed curves indicate 68% and 90% highest probability density regions. The top and right distributions are the 1-dimensional probability density distributions. The values given by the other theories are plotted as squares: green – USDB, GSM, and CSM, red –SDPF-M and EEdf3 and purple – VS-IMSRG.

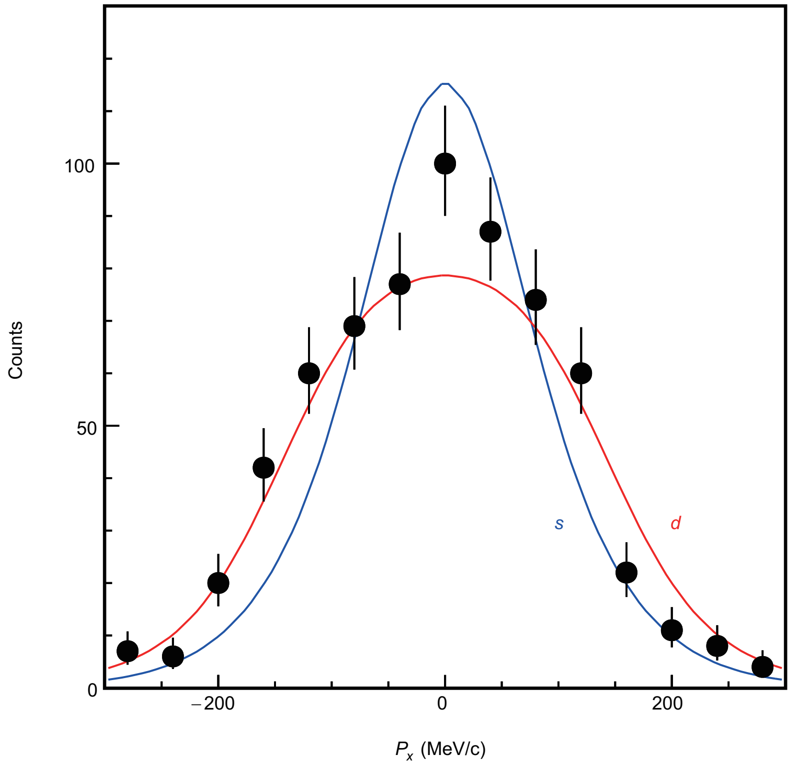

Extended Data Fig. 4 | Transverse momentum distribution of the ^{24}O+3n system in the rest frame of the ^{29}F beam. Events corresponding to the population of the ^{28}O ground state ($E_{012} < 0.08$ MeV and $E_{0123} < 0.8$ MeV) are shown by the data points. The blue and red solid lines represent the DWIA calculations, including the experimental effects for $s_{1/2}$ and $d_{5/2}$ proton knockout, respectively, whereby the distributions have been scaled to best fit experiment.

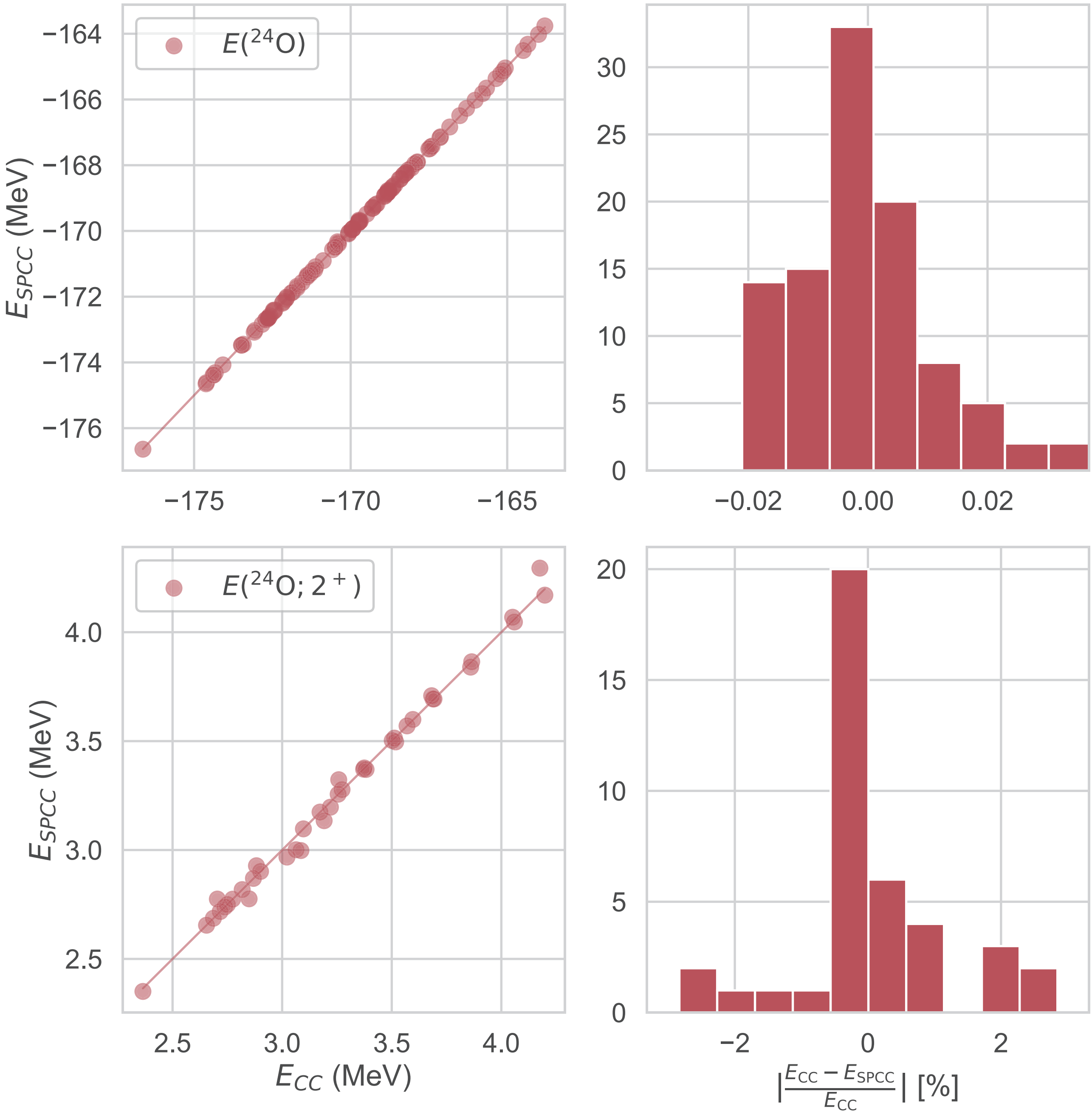

Extended Data Fig. 5 | Cross-validation of emulators. (Upper left panel) Total energies of ^{24}O computed with the coupled-cluster method in the CCSDT-3 approximation versus the SP-CC emulator for a validation set of 100 parameter samples. (Upper right panel) Distribution of residuals in percent. (Lower left panel) 2^+ excitation energies of ^{24}O computed with the coupled-cluster method in the EOM-CCSDT-3 approximation versus the SP-CC emulator for a validation set of 40 parameter samples. (Lower right panel) Distribution of residuals in percent.

Target	z	$\varepsilon_{\rm exp}$	$\varepsilon_{\rm model}$	$\varepsilon_{\rm method}$	$\varepsilon_{\rm emulator}$
$E(^2\mathrm{H})$	-2.2298	0.0	0.05	0.0005	0.001%
$r_p^2(^2\mathrm{H})$	3.9030	0.0	0.02	0.0005	0.001%
$Q(^2\mathrm{H})$	0.27	0.01	0.003	0.0005	0.001%
$E(^3\mathrm{H})$	-8.4818	0.0	0.17	0.0005	0.005%
$E(^4\mathrm{He})$	-28.2956	0.0	0.55	0.0005	0.005%
$r_p^2(^4\mathrm{He})$	2.1176	0.0	0.045	0.0005	0.05%
$E(^{16}\mathrm{O})$	127.62	0.0	0.75	1.5	0.5%
$r_p^2(^{16}\mathrm{O})$	6.660	0.0	0.16	0.05	1%
$\Delta E(^{22,16}\mathrm{O})$	-34.41	0.0	0.4	0.5	1%
$\Delta E(^{24,22}\mathrm{O})$	-6.35	0.0	0.4	0.5	4%
$E_{2^+}(^{24}\mathrm{O})$	4.79	0.0	0.5	0.25	2%
$\Delta E(^{25,24}\mathrm{O})$	0.77	0.02	0.4	0.25	—

Extended Data Table 1 | Error assignments used in the statistical analysis. Energies in (MeV), squared point-proton radii in (fm^2) and the deuteron quadrupole moment in (e^2fm^2). $\Delta E(^{25,24}\mathrm{O})$ is used in the Bayesian update step and the experimental target is from Hoffman et al.[24]. This observable is computed in particle-attached coupled-cluster theory[84] and does not involve an emulator.

Target	z	$\varepsilon_{\rm exp}$	$\varepsilon_{\rm model}$	$\varepsilon_{\rm method}$	$\varepsilon_{\rm emulator}$
$E(^2\mathrm{H})$	-2.2298	0.0	0.05	0.0005	0.001%
$r_p^2(^2\mathrm{H})$	3.9030	0.0	0.02	0.0005	0.001%
$Q(^2\mathrm{H})$	0.27	0.01	0.003	0.0005	0.001%
$E(^3\mathrm{H})$	-8.4818	0.0	0.17	0.0005	0.005%
$E(^4\mathrm{He})$	-28.2956	0.0	0.55	0.0005	0.005%
$r_p^2(^4\mathrm{He})$	2.1176	0.0	0.045	0.0005	0.05%
$E(^{16}\mathrm{O})$	127.62	0.0	0.75	1.5	0.5%
$r_p^2(^{16}\mathrm{O})$	6.660	0.0	0.16	0.05	1%
$\Delta E(^{22,16}\mathrm{O})$	-34.41	0.0	0.4	0.5	1%
$\Delta E(^{24,22}\mathrm{O})$	-6.35	0.0	0.4	0.5	4%
$E_{2^+}(^{24}\mathrm{O})$	4.79	0.0	0.5	0.25	2%
$\Delta E(^{25,24}\mathrm{O})$	0.77	0.02	0.4	0.25	—

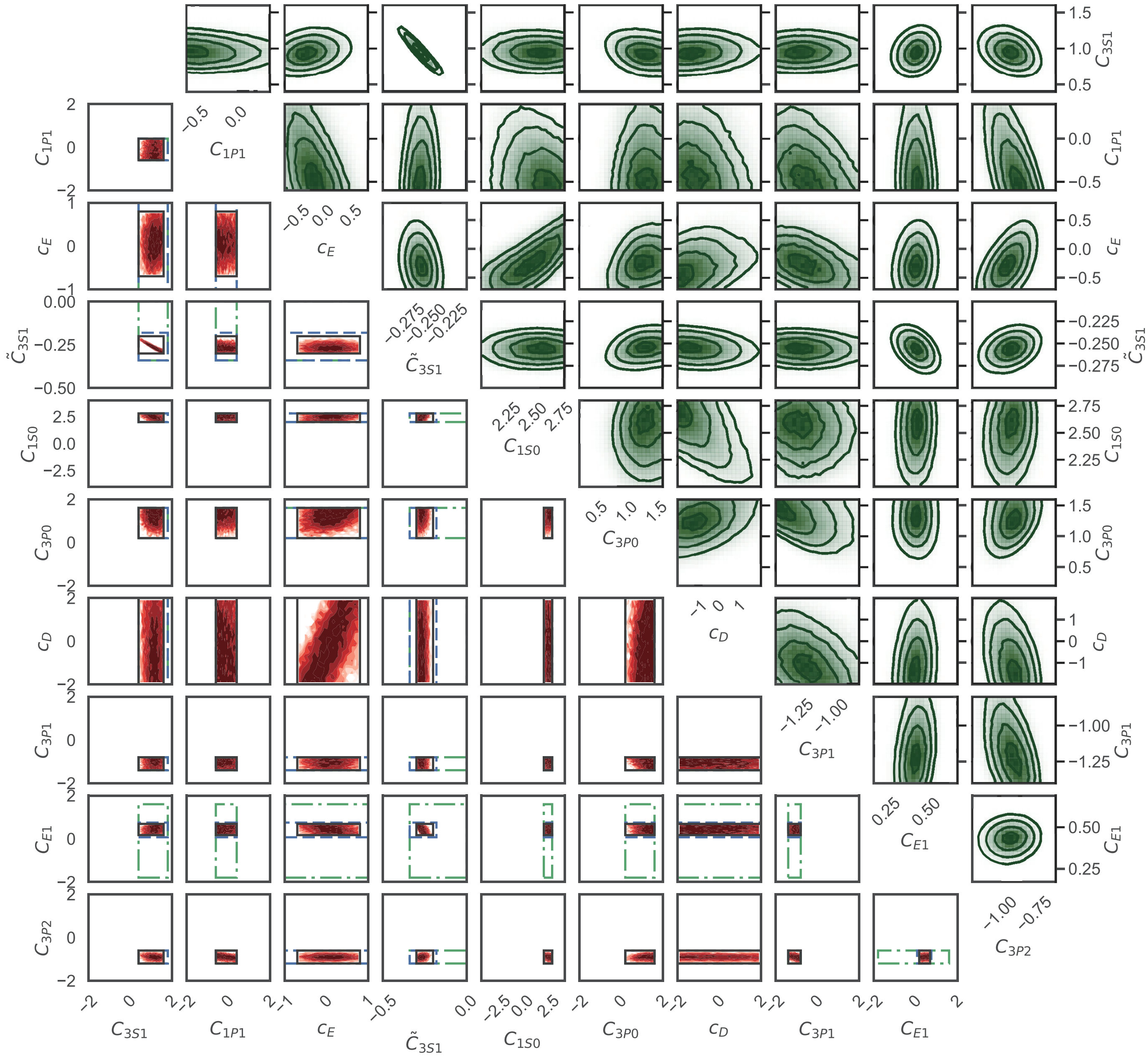

Extended Data Fig. 6 | History-matching waves and Bayesian posterior sampling. (Lower left triangle) The panel limits correspond to the input volume of wave 1. The domain is iteratively reduced and the input volumes of wave 2, 3, 4 are indicated by green/dash-dotted, blue/dashed, black/solid rectangles. The optical depths of non-implausible samples in the final wave are shown in red with darker regions corresponding to a denser distribution of non-implausible samples. (Upper right triangle) Parameter posterior pdf from MCMC sampling with the non-implausible samples of the history-matching analysis as starting points. We use an uncorrelated, multivariate normal likelihood function and a uniform prior bounded by the first wave initial volume. Note that the relevant posterior regions are small in some directions, but larger in others such as c_D and c_E.

Wave	Target set ($\mathcal{Z}$)	Number of active parameters	Number of input samples	NI samples fraction
1	*np* phase shifts	5–7	10^5–10^7	10^{-1}–10^{-4}
2	$A = 2$	7	10^8	$2.3 \cdot 10^{-4}$
3	$A = 2$–4	13	10^8	$3.4 \cdot 10^{-5}$
4	$A = 2$–4, 16–24	17	$5 \cdot 10^8$	$1.3 \cdot 10^{-6}$

Extended Data Table 2 | Definitions of history-matching waves used in this work. The np phase shifts correspond to six targets ($T_{\text{lab}} = 1, 5, 25, 50, 100, 200$ MeV) for $^1S_0$, $^3S_1$, $^1P_1$, $^3P_0$, $^3P_1$, $^3P_2$ partial waves. The $A = 2$ observables are $E(^2\text{H})$, $r_p(^2\text{H})$, $Q(^2\text{H})$, while $A = 3, 4$ are $E(^3\text{H})$, $E(^4\text{He})$, $r_p(^4\text{He})$. Finally, $A = 16 - 24$ correspond to $E(^{16}\text{O})$, $r_p(^{16}\text{O})$, the binding-energy differences $\Delta E(^{24,22}\text{O})$, $\Delta E(^{22,16}\text{O})$ and $E_{2^+}(^{24}\text{O})$.

Wave	Target set (Z)	Number of active parameters	Number of input samples	NI samples fraction
1	np phase shifts	5–7	10^5–10^7	10^{-1}–10^{-4}
2	$A = 2$	7	10^8	$2.3 \cdot 10^{-4}$
3	$A = 2-4$	13	10^8	$3.4 \cdot 10^{-5}$
4	$A = 2-4$, 16–24	17	$5 \cdot 10^8$	$1.3 \cdot 10^{-6}$

Parameter	median	68% credible region
$\tilde{C}_{\mathrm{1S0pp}}$	-0.343	$[-0.360, -0.327]$
$\tilde{C}_{\mathrm{1S0np}}$	-0.339	$[-0.352, -0.328]$
$\tilde{C}_{\mathrm{1S0nn}}$	-0.337	$[-0.349, -0.327]$
$\tilde{C}_{\mathrm{3S1}}$	-0.258	$[-0.272, -0.245]$
C_{1S0}	2.502	$[2.377, 2.785]$
C_{3P0}	1.343	$[1.217, 1.600]$
C_{1P1}	-0.273	$[-0.600, -0.115]$
C_{3P1}	-1.074	$[-1.199, -0.834]$
C_{3S1}	0.982	$[0.803, 1.160]$
C_{E1}	0.437	$[0.358, 0.512]$
C_{3P2}	-0.920	$[-1.032, -0.809]$
c_1	-0.740	$[-0.760, -0.721]$
c_2	-0.494	$[-0.645, -0.347]$
c_3	-0.645	$[-0.841, -0.456]$
c_4	0.958	$[0.861, 1.056]$
c_{D}	-0.460	$[-1.955, 0.175]$
c_{E}	-0.107	$[-0.471, 0.196]$

Extended Data Table 3 | Medians and 68% credible regions (highest-density intervals) from the Bayesian posterior pdf of χEFT model parameters obtained with MCMC sampling as described in the text.

Parameter	median	68% credible region
$\tilde{C}_{\mathrm{1S0pp}}$	-0.343	$[-0.360, -0.327]$
$\tilde{C}_{\mathrm{1S0np}}$	-0.339	$[-0.352, -0.328]$
$\tilde{C}_{\mathrm{1S0nn}}$	-0.337	$[-0.349, -0.327]$
$\tilde{C}_{\mathrm{3S1}}$	-0.258	$[-0.272, -0.245]$
C_{1S0}	2.502	$[2.377, 2.785]$
C_{3P0}	1.343	$[1.217, 1.600]$
C_{1P1}	-0.273	$[-0.600, -0.115]$
C_{3P1}	-1.074	$[-1.199, -0.834]$
C_{3S1}	0.982	$[0.803, 1.160]$
C_{E1}	0.437	$[0.358, 0.512]$
C_{3P2}	-0.920	$[-1.032, -0.809]$
c_1	-0.740	$[-0.760, -0.721]$
c_2	-0.494	$[-0.645, -0.347]$
c_3	-0.645	$[-0.841, -0.456]$
c_4	0.958	$[0.861, 1.056]$
c_{D}	-0.460	$[-1.955, 0.175]$
c_{E}	-0.107	$[-0.471, 0.196]$

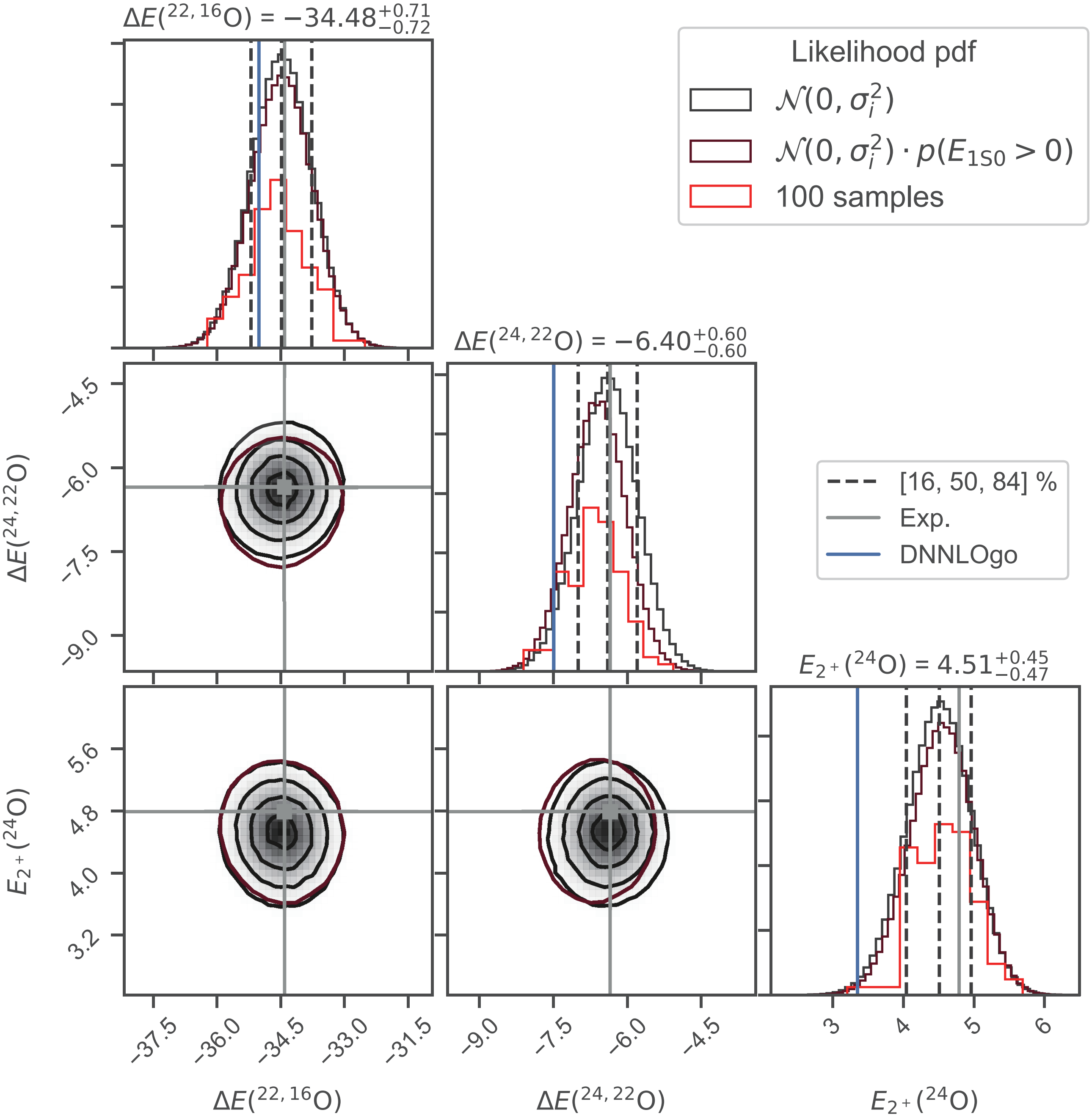

Extended Data Fig. 7 | Posterior predictive distributions for ^{16,22,24}O. MCMC samples of the posterior predictive distribution for selected oxygen observables. The black (maroon) histogram shows results obtained with an uncorrelated, Gaussian likelihood (including a discrete probability $p(E_{np,1S0} > 0|\theta) = 1$). The red histogram illustrates a low-statistics sample. The 68% credible regions and the medians are indicated by dashed lines on the diagonal, while the solid, vertical grey (blue) lines show the experimental target (prediction with the ΔNNLO$_{\mathrm{GO}}$(394) interaction).